A Computational Study on Melting Point of Si-Ge-Sn High Entropy Alloy

by

Ahmad M. Alqaisi

A Thesis Presented in Partial Fulfillment
of the Requirements for the Degree
Master of Science

Approved February 2023 by the
Graduate Supervisory Committee:

Houlong Zhuang, Co-chair
Qi-Jun Hong, Co-chair
Yang Jiao

ARIZONA STATE UNIVERSITY

May 2023

ABSTRACT

High-entropy alloys (HEAs) is a new class of materials which have been studied heavily due to their special mechanical properties. HEAs refers to alloys with multiple equimolar or nearly equimolar elements. HEAs show exceptional and attractive properties currently absent from conventional alloys, which make them the center of intense investigation. HEAs obtain their properties from four core effects that they exhibit and most of the work on them have been dedicated to study their mechanical properties. In contrast, little or no research have gone into studying the functional or even thermal properties of HEAs. Some HEAs have also shown exceptional or very high melting points. According to the definition of HEAs, Si-Ge-Sn alloys with equal or comparable concentrations of the three group IV elements belong to the category of HEAs. Thus, the equimolar components of Si-Ge-Sn alloys probably allow their atomic structures to display the same fundamental effects of metallic HEAs. The experimental fabrication of such alloys has been proven to be very difficult, which is mainly due to differences between the properties of their constituent elements, as indicated from their binary phase diagrams. However, previous computational studies have shown that SiGeSn HEAs have some very interesting properties, such as high electrical conductivity, low thermal conductivity and semiconducting properties. In this work, going for a complete characterization of the SiGeSn HEA properties, the melting point of this alloy is studied using classical molecular dynamics (MD) simulations and density functional theory (DFT) calculations. The aim is to investigate the effects of high Sn content in this alloy on the melting point compared with the traditional SiGe alloys. Classical MD simulations results strongly

indicates that none of the available empirical potentials is able to predict accurate or reasonable melting points for SiGeSn HEAs and most of its subsystems. DFT calculations results show that SiGeSn HEA have a melting point which represent the mean value of its constituent elements and that no special deviations are found. This work contributes to the study of SiGeSn HEA properties, which can serve as guidance before the successful experimental fabrication of this alloy.

DEDICATION

Dedicated to God Almighty,

My Teachers and Mentors,

My Family,

My Wife,

My Friends,

And all those who believe in me

ACKNOWLEDGMENT

I firstly thank Almighty God for giving me the will and power to finish this thesis successfully and strengthening me through the difficult times during this degree. I would like to express my gratitude to both of my mentors, Dr. Houlong Zhuang and Dr. Qi-Jun Hong for their faith in me, even during difficult times, and for their constant support and guidance which was vital to the success of this thesis. I learned a lot under each one of them and I'm grateful for the research opportunity they gave me, which contributed a lot to my scientific thinking and building my research experience. I would also like to thank my committee member, Dr. Yang Jiao, who also taught me a very useful class, for his valuable contribution and effort to review this work. I would also like to thank my family for their constant support and motivation, which always gave me the courage to continue and push forward with my career. Finally, I would like to thank my dear wife Sally Abu Laila, for her support, encouragement, motivation and helpful discussions, which not only helped and encouraged me to battle through difficult times and reach where I am today, but also contributed to my learning and scientific accuracy.

TABLE OF CONTENTS

Page

CHAPTER Page

LIST OF TABLES

Table Page

LIST OF FIGURES

Figure Page

Figure Page

A COMPUTATIONAL STUDY ON MELTING POINT OF SI-GE-SN HIGH ENTROPY ALLOY

1 THESIS OVERVIEW AND LAYOUT

1.1 High Entropy Alloys

Throughout human history, the discovery of new material always marked the beginning of a new era. One of these material types, metallic alloys, played a very important role in the development of society. To create a conventional alloy, one would need to decide on two components; the principal element and the minor element. The principal element serves as the base of the alloy. This base is usually chosen based on its attractive and useful properties and also based on its stability when combined with lower concentrations of other minor elements. In most cases, one principal element is chosen. The minor component is one or more elements that are added to the principal element with a very low concentration. Famous examples of these alloys where one of each component is present are Steel alloy (Iron base with minor concentrations of Carbon) and Brass alloy (Copper base with minor concentrations of Tin). There are almost thirty common alloy systems that are used regularly for a variety of applications. Alloys offer a wide range of properties and performances which explains their ubiquity and usage in many different areas. [1]. Although alloy design techniques and tools have hugely advanced from ancient eras to modern times, the main concepts of principal and minor elements stayed at the core of their design principle. The choice of principal elements and the control over the number and concentrations of each of the minor elements continued to progress with time, in search of new alloys that offer the best performance or suit a

specific application. With all this variety, conventional alloys still failed to be a suitable material for some highly needed applications, like high-temperature applications, energy production, or alloys with high strength and high toughness simultaneously [2]. One central problem is the lack of new principal elements that have the appropriate properties and stability. This defined a limit on the traditional design concept of conventional alloys. A change in the fundamental ideas was needed to progress the field [1-4] This was made by the advent of high entropy alloys (HEAs) in 2004 [5].

1.1.1 History and Definition

In 2004, professor Cantor with his team from the University of Oxford, and professor Jien-Wei Yeh from the National Tsing Hua University in Taiwan were working, at the same time, but independently, on a fundamental new idea of alloy design, that would revolutionize the field. A multi-principal element alloy, where instead of having a single base element as the main component of the alloy, you have multiple principal elements mixed in equimolar concentration in the same structure to create an alloy. The idea started with different motivations for the two research groups, but both of them focused on the unexplored regions of the multicomponent alloy phase diagrams, that is the regions where you have equ-atomic ratio of multiple elements, rather than one element as the base. Two papers from the research groups were published in that year and they marked the launch of multi-principal element alloys field (MPEs), later called high entropy alloys (HEAs) [5, 6]. HEAs were originally defined as an alloy with 5 or more principal elements with each element having a concentration of 5 to 35 atomic percent. Additionally, similar to conventional alloys, HEAs can contain minor concentrations of

other non-principal elements. This definition was later expanded to include alloys with even 3 principal elements and with higher atomic concentrations than 35%, but meets the other criteria of HEAs. An alloy base in HEAs is a specific combination of principal elements, and there are a vast number of them. This is due to the huge number of ways that r principal elements can be taken from n candidates, described by the equation

$$C_r^n = \frac{n!}{r!(n-r)!} \tag{1.1}$$

There are $n = 75$ stable elements that aren't toxic, radioactive, or noble gases, resulting in over 219 million new alloy systems with $3 \le r \le 6$ major elements [2]. Even if we followed the strict criteria of 5 elements or more, the number would still be huge. Also, unlike an elemental alloy base, which only gives one base per element, a combination of r specific elements HEA base can provide a variety of unique alloy bases by varying their concentrations. This makes the numbers even greater [4]. The high entropy refers to the high configurational entropy of random mixture of elements in these alloys, which helps in stabilizing the ideal solid solution [5]. The second definition of HEAs relies on the concept of entropy. A HEA is defined as an alloy that has a configurational entropy greater than $1.61R$ in its random solution state, where R is the gas constant.

$$\Delta S_{mix} \ge 1.61R \tag{1.2}$$

Entropy in thermodynamics is a state function and a parameter that describes randomness. Entropy of a system is given by

$$S = k \ln W \tag{1.3}$$

where k is Boltzmann constant, related to the gas constant R, and W is the total number of microscopic states in the macroscopic system. It can be seen that as the number of microscopic states increases, the entropy value of the system increases, and entropy is a measure of the number of microscopic states of the system. When the heat of mixing is ignored, the increase in the entropy of the system which is caused by the different configurations of the atoms of different alloying elements is called *configurational entropy*, *hybrid entropy*, or *mixing entropy*. When the solid solution is composed of n kinds of atoms, the configurational entropy is given by

$$\Delta S_{conf} = -R\sum_{i=1}^{n} c_i \ln c_i \tag{1.4}$$

where c_i is the element concentration in atomic percent. This expression reaches its maximum value when $c_1 = c_2 = ...c_n$ and the expression become

$$\Delta S_{conf} = R\ln n \tag{1.5}$$

where n is the number of components in the system. It can be seen that the greater the number of components in a system, the higher the mixing entropy. From here, materials or alloys can be classified into three main categories: (1) Low entropy alloys: $\Delta S_{conf} \le 0.69R$, containing 1 or 2 main elements. (2) Medium entropy alloys (MEA): $0.69R \le \Delta S_{conf} \le 1.61R$, containing 2-4 main elements. (3) High entropy alloys (HEA): $\Delta S_{conf} \ge 1.61R$, containing five main elements at least. This lays out a criterion and a definition of HEAs. For many years, HEAs have been studied under the classic definition of 5 or more elements with a single-phase solid solution. But now the limits

have been steadily broken as our understanding of HEA has evolved. New classes of HEAs and other related concepts are arising, like non-equimolar multiphase solid solution alloys, high entropy ceramics, and complex concentrated alloys (CCAs) [4].

1.1.1 Phase formation and selection rules

Different phases of a material are controlled by thermodynamic and kinetic factors. The Gibbs free energy ΔG is an important quantity in calculating the phases of a material, and it is defined as

$$\Delta G = \Delta H - T\Delta S \tag{1.6}$$

where ΔH is the enthalpy, T is the temperature, and ΔS is the entropy. When mixing different elements, the Gibbs free energy of mixing comes into play

$$\Delta G_{mix} = \Delta H_{mix} - T\Delta S_{mix} \tag{1.7}$$

Although there are many possible states in the solid state of an alloy, the equilibrium state is the one with the lowest free energy of mixing, according to the second law of thermodynamics. In HEAs, the original idea was that the very high entropy of mixing of the various elements in the HEA will stabilize the formation of solid solution against any other phases like intermetallic compounds [5]. This effect was called constantly as the "high entropy effect", which was at the core of the definition of HEAs, high mixing entropy to enhance the formation of solid solution by reducing Gibbs free energy, especially at high temperatures [3]. In the original studies, HEAs were modeled as ideal solutions, in that case the expression for mixing entropy ΔS_{mix} in Eqn. 1.7 is the same

expression given in Eqn. 1.5. The high entropy effect has been the main design philosophy of HEAs since their discovery, and it can be translated as follows

$$TS_{sys} \gg \max\{|H_i|\} \quad (i = 1, 2, ..., m) \tag{1.8}$$

Where S_{sys} is the configurational entropy of mixing of the alloy system and H_i is the formation enthalpy of the i th phase, assuming m possible phases in total [3]. However, in reality, other kinds of phases were detected in HEAs, like intermetallic and metallic glasses, this means that ΔS_{mix} cannot be used as the sole parameter in the design of HEAs. The phase formation rules of HEAs are an extension of the Hume-Rothery rules for conventional alloys (crystal structure, atomic size difference, valence, and electronegativity) and also other additional empirical criteria developed by others researchers.

1.1.2.1 Mixing entropy ΔS_{mix} and mixing enthalpy ΔH_{mix}

The main thermodynamic quantities in the HEAs criteria are the mixing entropy and enthalpy. Mixing entropy is in the core of the HEAs definition, and according to Eqn. 1.5, the greater the number of components in the alloy, the greater the mixing or configurational entropy, the lower the Gibbs free energy of mixing. In the original definition, an equ-atomic multicomponent alloy of five or more having a mixing entropy of $\Delta S_{conf} \geq 1.61R$ formed a high entropy alloy. However, mixing entropy alone is not sufficient to stabilize the solid solution phase in every system. The mixing enthalpy ΔH_{mix} must also be taken into account. ΔH_{mix} is given by [7]

$$\Delta H_{mix} = \sum_{ij\, i \neq j} \Omega_{ij} c_i c_j \tag{1.9}$$

Where $\Omega_{ij}=4\Delta H_{mix}^{AB}$ and ΔH_{mix}^{AB} are the mixing enthalpies of binary A-B alloys as calculated according to Miedema's semi-empirical model. It has been found empirically that in order to form a complete solid solution, should be between -10 and -5 KJ/mol [8].

1.1.2.2 δ, $\Delta\chi$ and *VEC* parameters

The Hume-Rothery rules describe the effect of atomic size difference, electronegativity difference, and valence electron concentration on the formation of solid solution between elements. For HEAs, where there is no clear distinction between solvent and solute components, the Hume-Rothery rules were modified and extended. According to this criterion, the average atomic size difference is defined as [9]

$$\delta=\sqrt{\sum_{i=1}^{n}c_i\left(1-\frac{r_i}{\bar{r}}\right)^2} \tag{1.10}$$

Where n is the total number of components i, each having a concentration and a radius c_i and r_i respectively. $\bar{r}$ is the average of atomic radius of the alloy: $\bar{r}=\sum_{i=1}^{n}c_i r_i$. It can be found that generally the formation of solid solution phase requires a $\delta\leq 6.5\%$. The electronegativity difference $\Delta\chi$ is given by [10]

$$\Delta\chi=\sqrt{\sum_{i=1}^{n}c_i(\chi_i-\bar{\chi})^2} \tag{1.11}$$

Where the average electronegativity $\bar{\chi}=\sum_{i=1}^{n}c_i\chi_i$. The valence effect in the Hume-Rothery criterion describes the effect of valence electron concentration on the stability of solid solution. When the atomic valences of the components are close, the component's solid solubility is higher, and the solid solution in the alloy is relatively stable. When the

valence electron concentration varies or exceeds a certain threshold, the bond between the components becomes disordered, reducing the solid solution's stability and favoring the formation of intermetallic compounds. The VEC of the alloy is defined as

$$VEC = \sum_{i=1}^{n} c_i (VEC)_i \tag{1.12}$$

Where $(VEC)_i$ is the valence electron concentration of the i-th component of the alloy. VEC is a useful criterion to predict the crystal structure of HEAs, mainly the stability of FCC and BCC structures in HEA. It is considered that when $VEC \geq 8.6$, the FCC solid solution phase is stable, while when $VEC < 6.87$, the BCC solid solution phase is relatively stable [10].

1.1.2.3 Ω Criteria

The Ω parameter was proposed relate between the criteria and the mixing entropy criteria [9]. It is related to the established assumptions of Takeuchi and Inoue that relates the free energy change of alloy to the free energy change in the liquid state. The Ω parameter can be written as

$$\Omega = \frac{T_m \Delta S_{mix}}{\left|\Delta H_{mix}\right|} \tag{1.13}$$

Where $T_m = \sum_{i=1}^{n} c_i \left(T_m\right)_i$ and $\left(T_m\right)_i$ is the melting point of the i-th element. The critical value of the parameter is 1. If $\Omega > 1$, the effect of mixing entropy on the formation of solid solution exceeds that of mixing enthalpy, and the alloy tends to form a solid solution.

1.1.2 Characteristics and applications of HEAs

HEAs have four core effects associated with them, which are: (1) the high entropy effect, (2) the severe lattice distortion effect, (3) the sluggish diffusion effect, and (4) the "cocktail" effect [11] [12]. The high entropy effect describes the huge influence of configurational entropy on the stability of solid solution phases against other phases. The maximized mixing entropy (configurational entropy) in HEAs tends to lower the Gibbs free energy of the solid solution phase and increase its chance of appearing as a stable phase compared to other phases. The lattice distortion effect originates from the mismatch of atomic sizes between different elements that form the HEA, causing lattice strain and stress. The sluggish diffusion effect slows the diffusion and phase transformation kinetics in HEAs. That's mainly due to the different local environments that the atom faces when it jumps into a vacancy (different bonding and local energies), unlike in conventional alloys where most of the time, the local atomic configuration in the site before and after are the same. The cocktail effect refers to the surprising and exotic properties that one gets from the complex mixture of the many different elements that compose the HEA lattice. The macroscopic properties of HEAs are not only the average properties of their components but also, the interaction between the different elements can produce excess quantities that are more than the average quantities predicted by the simple mixture.

Because the majority of HEAs have advantageous mechanical properties, such as high hardness values [13-15], yielding stresses , fatigue resistance [16, 17], and irradiation resistance [18, 19], a large portion of the research effort has gone into studying their mechanical properties for structural applications. However, some HEAs also show

interesting functional properties, such as magnetic properties, semiconducting properties, and superconductivity [20], and these properties have received significantly less research attention. For example, superparamagnetic properties have been reported for Ti0.8CoCrCuFeNi and TiCoCrCuFeNi HEAs [21]. Superconducting properties were also reported for several HEAs, like HfNbTaTiZr and Ta–Nb–Hf–Zr–Ti [22]. In regards to semiconducting properties, studies have discovered that when alloying elements Ge, Pb, and Mn are successively added to the SnTe binary alloy to form HEAs, the valence bands and bandgaps in the HEAs are modified as a result of the cocktail effect [23]. The ternary Sn-Ge-Te HEA, in particular, showed a significant reduction in the bandgap without significantly altering the original band structure. The Sn-Ge-Pb-Mn-Te HEA, on the other hand, had a wider bandgap as well as more flattened valence bands in the band structure than the binary SnTe alloy [23].

1.2 SiGeSn High Entropy Alloy System

The elements Si, Ge and Sn make a famous set of binary and ternary alloys that have been heavily investigated lately, due to their importance and applications in optoelectronic devices. Silicon (Si) and Germanium (Ge) are elemental semiconductors and as elements, they have many similar properties. This makes them easier to form an alloy with a solid solution phase and a high concentration of one of them as the minor element. The element Tin (Sn) however, while existing in the same periodic element group as Si and Ge, has different properties than the other two elements. In the conventional alloying scheme, this makes either Si or Ge the principal element if Tin (Sn) is present in the alloy, due to its different properties. The binary and ternary conventional

alloys made of these three elements have one very attractive electronic property, which is the ability to achieve a direct-bandgap material, which is not present in the elemental semiconductor form of these elements. The binary alloys Si-Sn and Ge-Sn have a tunable or a controlled bandgap as the concentration of Sn varies. It has been reported that a Tin (Sn) concentration of 8% changes the bandgap of Ge from indirect-bandgap to direct-bandgap and lowers its value [24]. The same behavior of Tin-concentration controlled bandgap is also found in the ternary SiGeSn alloys. [25]. Because of their similar properties, the phase diagram of Si-Ge binary system shows full solubility of Ge in any concentration of Si, resulting in Si-Ge alloy being a solid-solution alloy [27]. This makes their experimental fabrication a doable process and indeed, many Si-Ge have been developed for a variety of applications, including near-infrared devices [28]. However, when Sn is included in either the binary or the ternary combination, the fabrication of such alloys becomes very difficult [31].. The main reason of that as mentioned earlier is the striking differences between the properties of Sn compared to the two others, which reflects in their binary phase diagrams having a very low solubility limit [26].. In the Si-Sn and Ge-Sn binary phase diagrams, the thermodynamic solubility limit at room temperature is below 1%. [29, 30]. Many innovative experimental methods were developed to fabricate ternary SiGeSn alloys with the highest Tin concentration possible [32] [33]. But still, there is no defined upper limit for the concentration of Tin in this alloy. Studies on this structure, for the most part, included one principal element such as Si with a very high concentration such as 70%, and the other two elements as minor elements with low concentration to tune the ternary alloy properties. The electrical [34,

36, 37], optical [35], and mechanical [34] properties of this ternary alloy have been investigated extensively in the literature, but, the Tin concentrations in all of these studies have not exceeded 10%. By definition, in the Si-Ge-Sn ternary diagram, alloys with these concentrations where one element has the dominant concentration are present in the corners of the phase diagrams. There is another form of this alloy that resides in the center of the phase diagram. This form has an equ-atomic concentration of these three elements ($Si_{0.3}Ge_{0.3}Sn_{0.3}$) and it can be called a high entropy alloy. In contrast, little to no studies have been done on this form of this alloy. The term "high entropy alloy" has never been used for Si-Ge-Sn in scientific literature. This high entropy form has never been synthesized experimentally due to the difficulties in incorporating high Tin concentrations with Si and Ge. Recently, using density functional theory and molecular dynamics simulations, Duo Wang et al. (2019; 2020) studied the electronic [38] and thermoelectric [39] properties of SiGeSn HEA, and have shown that this alloy has no chemical short-range order and remains semiconducting with a bandgap of 0.38 eV, which makes it promising for midinfrared optoelectronic applications. Also, these studies have shown that the SiGeSn HEA has high electrical conductivity and low thermal conductivity, which makes it a candidate for high thermoelectric (TE) applications at room temperature.

1.3 Melting Temperature Calculation

Melting temperature T_m is one of the fundamental and important property for any compound and knowing its value is a critical information in many applications [40-45].

Many computational methods have been developed for the theoretical prediction of melting temperature and they have been based on different computational approaches and with different levels of accuracy in describing the atomic interactions. Melting itself as a phenomenon is defined as the phase transition from a solid to a liquid phase. Thermodynamically, the melting temperature can be also defined as the temperature where the free energy of the solid is equal to the free energy of the liquid. While it is a common occurrence in everyday life, its atomic complexity is such that a clear physical explanation of its nature and, more importantly, dynamics is still absent. The methods for melting temperature calculation can be classified into two groups. The first class of methods are "direct" methods and the second is the free-energy methods. In the direct methods, the melting phenomena is directly simulated: the melting temperature is approached by the evolution of the solid and/or the liquid involved in the phase transition. Commonly used examples of these methods include the large two-phase coexistence method [46-52] and the fast-heating methods (Z-method) [42, 43, 53, 54] . In the two-phase method, a simulation of coexistence of the two phases, liquid and solid is carried out. The goal is to have a stable solid-liquid coexistence whose temperature is naturally the melting temperature. The simulation cell is split in half, with one half containing atoms in a solid structure and the other containing identically dense atoms from a liquid simulation of the same system. A fraction of the liquid phase will solidify if the system as a whole is at a temperature just below the melting point, producing the necessary latent heat. This warms the system up to the melting point since it is closed (NVE). The latent heat needed to melt the solid will also cool the system down if it is

over the melting point. The disadvantages of this approach include the requirement for big systems (both sides must be made up of a sufficient number of atoms), as well as a significant number of simulation steps, which is a frequent issue with the melting process. The other common method is the Fast-heating method, where an attempt to mimic the measurement of melting points in frequent experiments is done. A small solid cell is heated to a low temperature to begin the process. Then, as the temperature progressively rises, the atoms begin to move more quickly. The crystal melts when the temperature reaches a certain point. Because melting causes a temperature reduction due to the latent heat, it is simple to calculate the melting temperature. The procedure is equally simple as the two-phase method and uses only half the number of atoms in the simulation cell. The system must still go through a significant number of simulation steps to completely melt, though. In the free energy methods [55-57], the melting temperature is found by locating the intersection of the two free energy curves, which depends on independent calculations of the free energies of the solid and the liquid. The hardest to calculate among them is the liquid-state free energy [58]. This category includes methods like thermodynamic integration and two-phase thermodynamics methods.

1.4 Aims of this work

In this work, we study the melting properties of the binary SiGe alloy and the ternary not-yet synthesized SiGeSn high entropy alloy using classical molecular dynamics simulations and density functional theory calculations. We investigate the effect of the high Sn concentration on the melting point of the conventional SiGe binary

alloy system and the validity of the current interatomic potential models to simulate the melting of both the binary system and ternary high entropy system.

2 THEORETICAL REVIEWS OF COMPUTATIONAL METHODS

The aim of this chapter is to provide a theoretical background of the used computational methods in this thesis. The topics covered in section 1 and 2 of this chapter have been covered in great details in many standard textbooks. Our review follows references: [59, 60]. Section 3 and 4 introduces the used codes in this thesis

2.1 Molecular Dynamics Simulations

Molecular Dynamics (MD) Simulations is a computer simulation method that is used to calculate the motion of atoms in a system based on classical mechanics laws, mainly Newton's law of motion

$$\vec{F} = m\vec{a} \tag{1.14}$$

where $\vec{F}$ is the force exerted on the particle, m is the mass of the particle, and $\vec{a}$ is the acceleration of the particle. Trajectories of the system that describe the acceleration, velocity, and positions can be obtained by integrating Newton's equations of motions, from there, many properties of the system can be calculated by applying statistical mechanics theorems. The macroscopic behavior of any system is related to the average microscopic properties of the atoms constituting the system, because of that, MD simulations are a powerful tool to study the properties of materials from their atomic interactions. Calculation of the forces on the atoms requires a knowledge of the model that governs their interactions, then using classical mechanics laws again

$$F = -\vec{\nabla}U(\vec{R}) \tag{1.15}$$

where $U(\vec{R})$ is the potential energy function that describes the interaction, and $\overrightarrow{\nabla}$ is the gradient, which represents the spatial derivative. In MD simulations, atoms are considered the lowest level of detail, disregarding electrons and nuclei. Because electrons and nuclei, which are the source of the interatomic interactions, are ignored, the need to generate an empirical potential energy function arises, also magnetic and electronic properties disappear for the same reason.

Numerical integration is carried to solve newtons equations of motion for obtaining motion trajectories, in the form

$$m\frac{d^2\vec{r}}{dt^2} = -\overrightarrow{\nabla}U(\vec{R}) \tag{1.16}$$

where $\vec{r}$ is the position of the particle and $\frac{d^2\vec{r}}{dt^2}$ represents the acceleration $\vec{a}$ of the particle.

The procedure in MD simulations goes as follows: input the initial structure of your system, determine the interaction model, calculate the forces exerted on each atom in your system, integrate Newton's Equations of motions to calculate the velocity and acceleration of each atom, obtain the motion trajectories of the system, and then compute desired properties from these trajectories.

2.1.1 Interatomic Potentials

One of the most important aspects of MD simulations is the use of accurate energy functions to model the system. There are many potentials to choose from, with different levels of accuracy and complexity. In general, these functions can be classified into three main types: empirical interatomic potentials, semi-empirical interatomic

potentials, and *Ab-Initio* interatomic potentials. In empirical interatomic potentials, the values for the parameters of the energy function are generated from experiments, like IR spectroscopy, Raman spectroscopy, ...etc., or quantum mechanical *Ab-initio* calculations. Some examples of this class of functions are Tersoff potential, Stillinger-Weber potential, Environment Dependent Interatomic Potential (EDIP), and Reactive force field (ReaxFF). Semi-empirical interatomic potential depends on parameters that are generated empirically, and also on other terms which are directly calculated from quantum mechanical arguments without the need for any other source. A famous example of this kind of potential is the Embedded Atom Method (EAM) potential, which is used commonly for metals. Ab-initio interatomic potentials calculate atomic interactions from electronic interactions.

2.1.1.1 Pair potentials

Pair potentials are the simplest kind of interatomic potential that can be used to study material properties. These functions approximate the full cohesive energy of the N-atom system to simply the pair-wise sum of two-atom pair interactions only, ignoring all other higher-order terms (triplet interaction, four atoms interaction, etc.) that result from the atom interacting with other atoms that are far away.

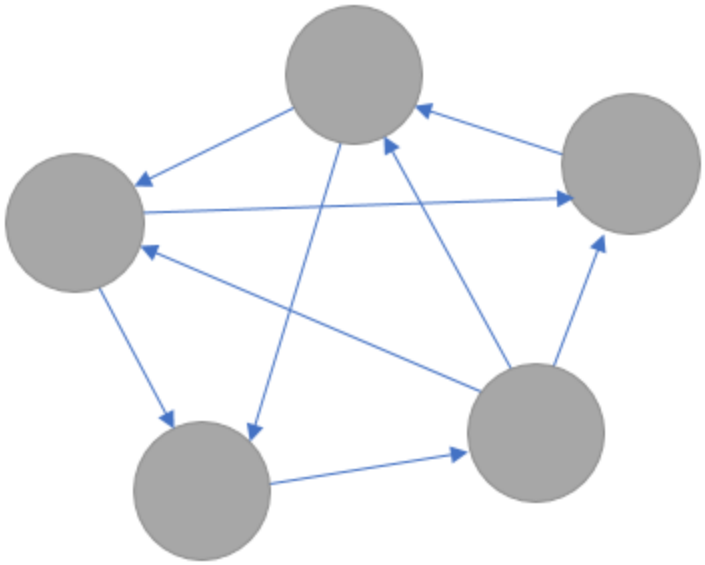

Figure 1. Illustration of pair potential interactions

Pair potentials are typically used to study and model inert gasses, but also useful sometimes to study the properties of simple oxides or spherical molecules. Pair potentials can be written in the general form

$$U = \frac{1}{2}\sum_{i=1}^{N}\ \sum_{j=1}^{N}\phi_{ij}(r_i, r_j) \tag{1.17}$$

Where $\phi_{ij}(r_i, r_j)$ is a function of the atomic positions that represent the interaction between the pair of atoms (i, j), located at r_i and r_j, respectively. Since this is energy that we are talking about, $\phi_{ij} = \phi_{ji}$. A typical example of the pair potentials is the Leonard-Jones interatomic potential, which was initially developed for inert gas. This potential contains an attractive term that represents a Van der Walls type of bonding,

strongly dominating at long distance, and a repulsive term that represents the interaction of the electron clouds and the Pauli exclusion principle, dominating at short distances

$$U_{LJ}(r_{ij}) = \sum_{i} \sum_{j \neq i} 4\varepsilon_{ij} \left[\left(\frac{\sigma_{ij}}{r_{ij}} \right)^{12} - \left(\frac{\sigma_{ij}}{r_{ij}} \right)^{6} \right] \tag{1.18}$$

Where the adjustable parameters, ε_{ij} and σ_{ij}, represent the "depth" of the energy well, and the characteristic distance between the two atoms, respectively. These constants are obtained empirically, by fitting materials properties with experiments.

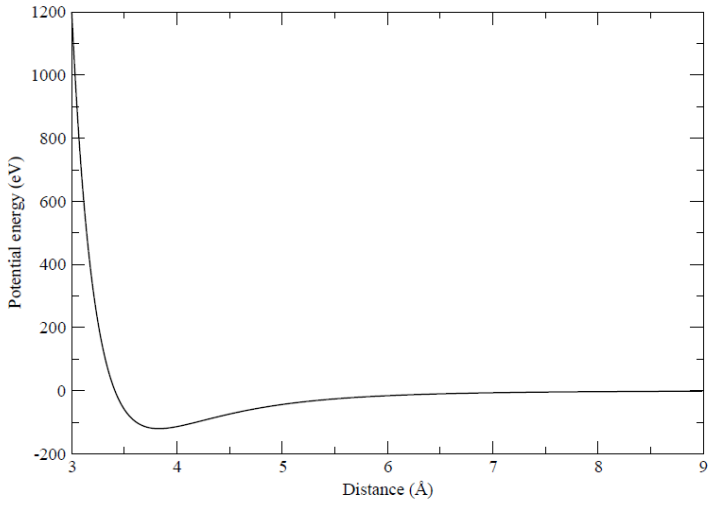

Figure 2. Leonard-Jones potential energy vs distance curve

The Leonard-Jones potential is used commonly because it has the feature of being a simple energy function but yet can describe central–force interatomic interactions in a good manner. While it was developed to describe the general interaction between closed-shell atoms, it has been used to model almost everything, including being part of the many-body potentials and empirical force fields

2.1.1.2 Three-body potentials

In covalent solids, such as silicon, it is not enough to describe the energies as a simple pair-wise sum of the atomic interactions; since the bonding between the atoms is highly directional. The interatomic potential for these materials should contain some angular-dependent terms to reflect the fact of the strong directionality of bonding. Three-body potentials include a pair-potential that only depends on the distance between two atoms, and also terms that depend on the angles between the bonds, they can be written in the general form as

$$U = \frac{1}{2}\sum_{i=1}^{N}\sum_{j=1}^{N}\phi_{ij}(r_i, r_j) + \sum_{i=1}^{N}\sum_{j\neq i}^{N}\sum_{k>j}^{N}\phi_{ijk}(r_{ij}, r_{ik}, \theta_{ijk}) \qquad (1.19)$$

Where the first term is the simple pair-potential, and the second term is an angular-dependent term that depends upon the angle between the vector distances of the two bonds. A very well-known potential of this kind for silicon is the Stillinger-Weber potential, which was initially developed to model the tetrahedral form of the solid, but later extended to many other elements and compounds. In Si tetrahedral, each atom is surrounded by four other Si atoms, with the equilibrium angle between the bonds set to the standard 109.47°. The Stillinger-Weber potential takes the general form

$$U = \sum_{i}\sum_{j>i}\phi_2(r_{ij}) + \sum_{i}\sum_{j\neq i}\sum_{k>j}\phi_3(r_{ij}, r_{ik}, \theta_{ijk}) \qquad (1.20)$$

Where ϕ_2 and ϕ_3 are the two and three-body potentials respectively, and written as

$$\phi_2(r_{ij}) = \begin{cases} \varepsilon_{ij}A_{ij}\left[B_{ij}\left(\frac{r_{ij}}{\sigma_{ij}}\right)^{-P_{ij}} - \left(\frac{r_{ij}}{\sigma_{ij}}\right)^{-q_{ij}}\right]\exp\left(\frac{\sigma_{ij}}{r_{ij} - a_{ij}\sigma_{ij}}\right), & r_{ij} < a_{ij}\sigma_{ij} \\ 0, & otherwise \end{cases} \qquad (1.21)$$

$$\phi_3(r_{ij}, r_{ik}, \theta_{ijk}) = \begin{cases} \varepsilon_{ijk}\lambda_{ijk} \exp\left(\frac{\gamma_{ij}\sigma_{ij}}{r_{ij} - a_{ij}\sigma_{ij}} + \frac{\gamma_{ik}\sigma_{ik}}{r_{ik} - a_{ik}\sigma_{ik}}\right) \times (\cos\theta_{ijk} + \cos\theta_{0ijk})^2, & r_{ij} < a_{ij}\sigma_{ij} \text{ and } r_{ik} < a_{ik}\sigma_{ik} \\ 0, & \text{otherwise} \end{cases} \quad (1.22)$$

The parameters $A_{ij}, B_{ij}, p_{ij}, \sigma_{ij}, \varepsilon_{ij}$ and $\varepsilon_{ijk}, \lambda_{ijk}, \sigma_{ij}, \gamma_{ij}, a_{ij}, \sigma_{ik}, a_{ik}, \gamma_{ik}, \theta_{0ijk}$ are adjustable parameters for the pair and triplet interactions of i and j, and i, j, and k respectively, which can found by fitting to experiment. The challenge in three-body potentials is that there are much more three-body terms than two-body terms. Even though these potentials tend to very accurately describe the properties of materials which they were designed for, they are typically limited to those materials; for example, The Stillinger-Weber potential works well for the perfect tetrahedral solid, but not at all well for the liquid, nor for any other solid structures. In general, Three-body potentials are used primarily for covalent materials like Si or mixed metallic-covalent systems like Mo.

2.1.1.3 Bond-order potentials

Bond-order potentials offer a good and flexible model to describe the effects of the environment on the bonding between atoms, by taking into consideration a quantity called the *bond-order*. The bond-order is related to the strength of the bond, such that a higher bond-order means in general stronger bonding. So, for example in C-C bonding, a single bond would be the weakest of the bonds that can form and triple would be the strongest and the bonding with higher bond-order. So, in general, bond-order depends on the local coordination around an atom i.e., the number of nearest neighbors, Z. Bond-order potentials can be represented by the general form

$$E_i = \frac{1}{2}\sum_{j=1}^{Z}[qV_R(r) + bV_A(r)] \quad (1.23)$$

Where q is a parameter that depends on the local electronic density, $V_R(r)$ and $V_A(r)$ are repulsive and attractive interactions, respectively. Z is the number of nearest neighbors. Z is the bond order, which controls the strength of the chemical bond.

Tersoff potential is one of the widely used empirical interatomic potentials from the bond-order class. Proposed by Tersoff in 1988, based on a variation on the idea of bond order, this potential describes the many states of silicon. The Tersoff potential can be written in the general form as

$$U_{Tersoff} = \frac{1}{2}\sum_{i=j}[V_R(r_{ij}) + b_{ij}\,V_A(r_{ij})] \tag{1.24}$$

Where b_{ij} the bond order is proportional to the coordination number

$$b_{ij}\,\alpha\,\frac{1}{\sqrt{Z_{coor}}} \tag{1.25}$$

In other words, the bonding b_{ij} of atom i with atom j is reduced by the presence of another bond b_{ij}. The degree of weakening depends on where this other bond is and what is the angle. Although both terms depend only on distance, this type of potential usually has more than six parameters to be fitted. It has been widely used and applied to study silicon, but also can be applied to SiC, diamond, amorphous carbon, and hydrocarbons.

2.1.1.4 Embedded-atom model potentials

In metallic structures, the long-ranged electrostatic interactions between the atoms (ions) surrounded by an electron sea make it very difficult to model the system with only

a simple pair-potential. The Embedded-atom method (EAM) tries to capture this effect in metals by modeling the interactions as a pair-potential sum, and added to it also another term which is called “the embedding energy”. This term represents the electronic energy associated with “embedding” the atom in a homogenous electron gas with a density ρ. The assumption here is that the environment of each atom is a nearly uniform electron gas. The EAM potential can be written as

$$U_{EAM} = \sum_{i<j}^{N} U_{ij}(r_{ij}) + \sum_{i}^{N} F_i(\rho_i) \tag{1.26}$$

Where U_{ij} is a pair-potential, and $F_i(\rho_i)$ d is called the embedding energy and it depends on the electron density ρ_i

Figure 3. Illustration of the interactions in EAM potential. The left part represents the pair interaction while the right part represents the effective potential due to homogenous electron gas

2.1.2 Numerical integration

Newton’s Equations of motion represent 3N second order coupled differential equations, where N represents the number of particles or atoms in the simulation system. These equations would have to be integrated at each timestep to predict the change in

position of every atom and get the full simulation trajectory. This process of course is impossible to do exactly or analytically, so several numerical integration algorithms were developed to carry out this integration using the finite difference method

2.1.2.1 Verlet Algorithm

Proposed by Verlet, this is a relatively simple algorithm to carry out the numerical integration of the equations of motions. It starts from the Taylor expansion for the position forward and backward in time, by a time step of

$$\begin{aligned} r_i(t-\delta t) &= r_i(t) - v_i(t)\delta t + \frac{1}{2}a_i(t)\delta t^2 \\ r_i(t+\delta t) &= r_i(t) + v_i(t)\delta t + \frac{1}{2}a_i(t)\delta t^2 \end{aligned} \tag{1.27}$$

From the summation of these two equations, we get the equation

$$r_i(t+\delta t) = 2r_i(t) - r_i(t-\delta t) + a_i(t)\delta t^2 \tag{1.28}$$

Which is the equation employed in Verlet Algorithm for advancing the positions. The acceleration is determined at each time step from the force evaluation from the gradient of the potential. The velocities can also be determined by doing a finite difference estimate of the derivative

$$v_i(t) = \frac{r_i(t+\delta t) - r_i(t-\delta t)}{2\delta t} \tag{1.29}$$

Which is of course an important quantity relating to the calculation of the kinetic energy and conservation of the total energy. We can also see that the Verlet algorithm equation has a dependence on the positions before a timestep δt, i.e., $r_i(t-\delta t)$, for the first

timestep, this is found by using the first equation alone $t = 0$. The Verelt algorithm is a simple and easy-to-program method to carry numerical integration, and it yields reasonable results.

2.1.2.2 Velocity Verlet Algorithm

This is a variant of the Verlet algorithm but in it, we have a velocity-dependent term in the main equation

$$\begin{aligned} r_i(t+\delta t) &= r_i(t) + v_i(t)\delta t + \frac{1}{2m}F_i(t)\delta t^2 \\ v_i(t+\delta t) &= v_i(t) + \frac{1}{2m}\left(F_i(t) + F_i(t+\delta t)\right)\delta t \end{aligned} \tag{1.30}$$

We note here that the position at the time $t + \delta t$ only depends on quantities evaluated at t. From the position at the time $t + \delta t$ the force at $t + \delta t$ can be calculated, then the velocity $v_i(t + \delta t)$ can also be calculated.

2.1.2.3 Leap-Frog Algorithm

This is a modified version of the Verlet algorithm, where several modifications from the original form are made. The most important aspect is that the velocity is explicitly calculated here, but on the other side, the calculation of the positions and the velocities is not being done at the same corresponding times. The velocities are first calculated at the time $t + \frac{1}{2}\delta t$ in this algorithm, which is later used to calculate the positions, r, at time $t + \delta t$

$$r_i(t+\delta t) = r_i(t) + v_i(t+\frac{1}{2}\delta t)\delta t$$
$$v_i(t+\frac{1}{2}\delta t) = v_i(t-\frac{1}{2}\delta t) + a(t)\delta t \quad (1.31)$$

At the time t, the velocities can be approximated by the following relation

$$v_i(t) = \frac{v_i(t+\frac{1}{2}\delta t) + v_i(t-\frac{1}{2}\delta t)}{2} \quad (1.32)$$

2.1.3 Energy, Temperature and Pressure Control

Certain thermodynamic and kinetic criteria must be satisfied, first of all, to get the conditions that we want the system in, and secondly to check our simulation quality and reliability

2.1.3.1 Connection to thermodynamics

In molecular dynamics, after determining the initial positions of the atoms in the system, the system is given a random velocity distribution according to some velocity distribution, like for example Maxwell-Boltzmann distribution

$$\mathrm{P(v)} = \left(\frac{\mathrm{m}}{2\pi \mathrm{k_B T}}\right)^{1/2} \exp\left(-\frac{\mathrm{mv}^2}{2\mathrm{k_B T}}\right) \quad (1.33)$$

Or from a Gaussian distribution. for a system in which the potential energy only depends on the positions of each atom in the system, and not their velocities, the total energy is conserved. The clearest connection to thermodynamic quantities would be the expression for the average temperature of the simulation system, given by

$$\langle T \rangle = \frac{2\langle KE \rangle}{3Nk_B} \tag{1.34}$$

Where $\langle KE \rangle$ is the average kinetic energy of the system.

2.1.3.2 Ensembles

The choice of constraints and conditions during the simulation is carried by choosing a specific molecular dynamics ensemble to simulate the system in. In the microcanonical ensemble (NVE), we have the number of particles N, volume V, and the total energy of the system E constant, which represent standard molecular dynamics. The microcanonical ensemble represents an isolated system which if given enough time, reaches an equilibrium, and the temperature value will be almost constant with small fluctuation around a certain average. The conjugate properties of the chosen ensemble (Pressure and temperature) can vary. The limitation of this ensemble is that we don't have any temperature control. The velocity rescaling approach tends to keep the system in the microcanonical ensemble while having some temperature control of the system. The simplest way to force a system to a certain temperature is to rescale velocities. This is done according to the knowledge of the kinetic theory and average kinetic energy expression

$$\langle KE \rangle = \left\langle \frac{1}{2} m v^2 \right\rangle = \frac{3}{2} N k_B T \tag{1.35}$$

$$\langle v \rangle = \left(3\frac{Nk_B T}{m} \right)^{1/2} \alpha \; T^{1/2} \tag{1.36}$$

If the desired temperature is T_s then by rescaling velocities

$$\mathbf{v}^{new} = \sqrt{\frac{T_s}{T}}\,\mathbf{v} \tag{1.37}$$

Each time the temperature drifts away from the desired temperature, the velocity is rescaled again, and the system is left to equilibrate.

2.2 Density Functional Theory

The Schrodinger equation is the central equation in quantum mechanics that describes the electronic structure of atoms and molecules. When solving this equation, one looks to find the wave function of a system $\Psi(x_1, x_2, ..., x_n)$ that describes the systems, which is generally a function of position of the electrons. The wave function contains important information about the probability distribution of electrons in the system. The Schrodinger equation can be solved analytically only for simple entities like the Hydrogen atom. For any other element or molecule, the equation becomes a complicated many-body problem which can only be solved by numerical methods. Density Functional Theory (DFT) is a theoretical framework where the solution of the Schrodinger equation is approximated by replacing the wave functions by another simpler quantity, the electron density $n(r)$. DFT is one of the most used computational methods in physics, chemistry and materials science, and here, we outline its main principles

2.2.1 Thomas-Fermi model

Thomas and Fermi independently presented the first attempts to employ electronic density as a fundamental variable in an electronic structure computation in 1927. Thomas and Fermi came to the conclusion that one could estimate the distribution of electrons using statistical techniques. Another advancement for this approximation is the use of local relations to a system's electrical characteristics, which are approximated as a homogenous electron gas. This, sometimes known as the local density approximation, is essential to DFT. The main result of the Thomas-Fermi model is a formula for kinetic energy calculation from electron density:

$$T_{TF}[n] = C_F \int n^{5/3}(r)\, dr \tag{1.38}$$

Therefore, the total energy of an atom can be written as:

$$E_{TF}[n] = C_F \int n^{5/3}(r)\, dr - Z \int \frac{n(r)}{r}\, dr + \frac{1}{2} \iint \frac{n(r_1) n(r_2)}{|r_1 - r_2|}\, dr_1\, dr_2 \tag{1.39}$$

where the kinetic energy is the first term, the ion core repulsion is the second term, and the electron-electron interaction term is the third. Only the electron density is a factor in the equation for an atom's total energy. This equation has a drawback in that it ignores all exchange and correlation terms and fails with molecules.

2.2.2 Hohenberg-Kohn theorem

The possibility that electron density might significantly affect electronic computations was recognized by scientists. But up until Hohenberg and Kohn (1964) finally verified it with two theorems, it was amenable to formal proof. This provided a solid basis for choosing electron density as the main component of the DFT. The existence hypothesis and the variational theorem are the two hypotheses. The electron density determines the external potential, within a trivial additive constant, according to

Theorem 1 (existence theorem). For the ground state of a many-electron system, this theorem provides a direct mapping of the external electron potential to the electronic density. Theorem 2: Theorem of variation: For a trail density, such $n(r)$ and $\int n(r)\,dr = N$

$$E_0 \leq E_{V_{ext}}[n] \tag{1.40}$$

The ground state density minimizes the system's electronic energy, according to this theorem's variational principle for DFT.

2.2.3 Kohn-Sham method

DFT became a useful tool because to Kohn and Sham's invention of an indirect technique for the kinetic energy term. To accurately compute the kinetic energy, they did this by introducing orbitals. The issue was designed by Kohn and Sham so that the kinetic energy, T [n], is precise. According to Kohn and Sham, the total energy equation becomes:

$$E[n] = T_S[n] + J[n] + E_{XC}[n] + \int V_{ext}(r)\, n(r)\, dr \tag{1.41}$$

The benefit of this approach is that the remaining exchange-correlation term $E_{XC}[n]$ may be approximated by splitting the kinetic energy term $T[n]$, from the long range Hartree interactions. Although realistic estimates have been produced, the actual should be highly complex. The capability of this approach to solve problems iteratively till self-convergence is another benefit.

2.2.4 Local Density Approximation (LDA)

The Kohn-Sham approach makes it possible to compute the kinetic energy precisely; nevertheless, the exchange-correlation term still poses a challenge, and here is where the local density approximation (LDA) comes in handy. The kinetic energy was calculated using a local uniform electron gas in the Thomas-Fermi model. With the Kohn-Sham technique, this is no longer necessary because the exchange-correlation portion of the energy functional is handled by the local uniform electron gas in the LDA. The exchange-correlation energy's local density approximation

$$E_{XC}^{LDA} = \int n(r)\,\varepsilon_{XC}(n)\,dr \tag{1.42}$$

This approach can be used in situations where the electron density slowly varies across a de Broglie wavelength, and it becomes precise at this limit. Due to directional bonding, which is known to systematically over-bind, it is less useful in systems with significant energy gradients. For LDA, including the PBE approach, corrections and approximations have been applied to increase accuracy.

2.3 LAMMPS Molecular Dynamics Simulations Package

LAMMPS or the *Large-scale Atomic/Molecular Massively Parallel Simulator*, is a classical molecular dynamics (MD) simulation tool created by Sandia National Laboratories that is free and open-source. [61]. Using a range of interatomic potentials (force fields) and boundary conditions, it can simulate and model atomic, polymeric, biological, solid-state (metals, ceramics, oxides), granular, coarse-grained, or macroscopic systems. With just a few particles all the way up to millions or billions, it can simulate 2D or 3D systems. LAMMPS is now written in the C++ programming

language. LAMMPS integrates Newton's equations of motion for a group of interacting particles in the broadest meaning.

2.4 Vienna *Ab initio* Simulation Package (VASP)

The *Vienna Ab initio Simulation Package*, also know as (*VASP)* is a computer program for the first-principles modeling of atomic scale materials, such as electronic structure computations and quantum mechanical molecular dynamics [62, 63]. When solving the Kohn-Sham equations using density functional theory (DFT) or the Roothaan equations using the Hartree-Fock (HF) approximation, VASP computes an approximation to the many-body Schrödinger equation. There are also hybrid functionals that combine the Hartree-Fock strategy with density functional theory. In VASP, fundamental parameters like as the electronic charge density, local potential, and one-electron orbitals are expressed as plane wave basis sets. The projector-augmented-wave approach, norm-conserving or ultrasoft pseudopotentials, or both are used to characterize the interactions between the electrons and ions. VASP employs effective iterative matrix diagonalization methods, such as the residual minimization method with direct inversion of the iterative subspace (RMM-DIIS) or blocked Davidson algorithms, to ascertain the electronic ground state.

3 METHODS FOR MELTING TEMPERATURE CALCULATION

3.1 Z-Method

The Z-method is a novel technique that allows the computation of melting temperature of a material, based on a series of simulations in the microcanonical ensemble (*NVE*) [64-66]. To explain the rationale behind the Z-method, a basic definition of heterogenous and homogenous melting is needed. The melting process, as we usually observe it, is technically the so-called heterogenous melting, where melting is initiated due to inhomogeneities. But, under special conditions, it is possible that a solid melts in a homogenous way. It has been shown that if a crystal structure melts homogenously, it can be overheated significantly above its melting point T_m. However, there is a critical temperature over which it is impossible to heat a solid without also turning it into a liquid structure. That point is called the critical superheating temperature T_{LS}. Much research has gone into studying the physical interpretations and the criteria behind this critical temperature. Based on the concepts of homogenous melting and critical superheating, the Z-method was developed. The Z-method can be applied using classical or ab-initio molecular dynamics simulations. In the *NVE* ensemble, simulating a system at a temperature beyond its limit of superheating T_{LS} will cause it to melt, naturally, without any external intervention of the dynamics. When the system melts, the latent heat is removed from it, which will decrease its temperature to the temperature of the liquid state, which will be the melting temperature T_m. The pressure also increases due to the volume expansion that the system would experience if the volume wasn't fixed in this

case. This sudden change in the temperature and pressure due to melting of the system can be seen if we plot the isochore $T(P)$ of the system, and it will be an inflection that looks like a *Z-shaped curve*, hence comes the method name. This sudden transition usually divides the isochore plot into two lines or branches, the first called the *solid branch*, which the highest temperature on it represents T_{LS}, and the second is called the *liquid branch*, where its lowest temperature point represents T_m the melting temperature. By doing many simulations for the system in the NVE ensemble, and mentoring the isochore for each initial temperature, one could determine the melting point at a specific pressure $T_m(P_m)$. The intended pressure is chosen by changing the system volume, thus changing the density.

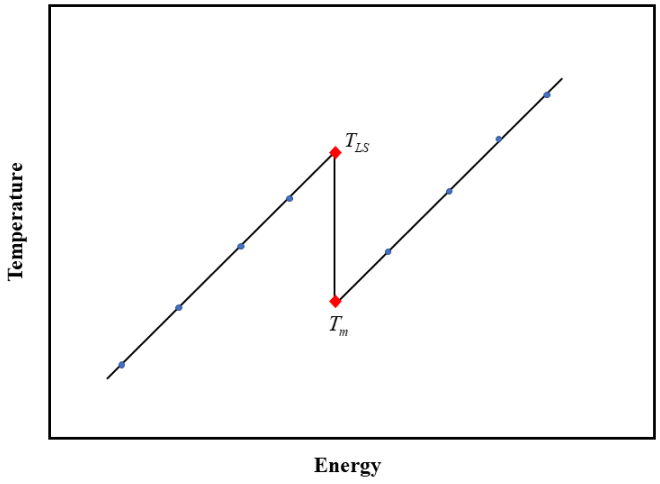

Figure 4. Schematic representation of the isochoric lines in Z-method simulations in the energy temperature plane.

3.1.1 Molecular Dynamics Simulations Setup in LAMMPS

All MD simulations were carried using the Large-scale Atomic/Molecular Massively Parallel Simulator (LAMMPS) and using the Stillinger-Weber (SW) many-body interatomic potential developed by Tomita et al. [67]. This interatomic potential was used successfully to calculate the phonon and heat-transfer properties of the SiGeSn systems. The parameters of this potential are described in Table 1. In order to imitate the SiGeSn HEA's crystal structure, we start with a particular quasirandom structure (SQS). Since its creation almost 30 years ago, the SQS approach has been widely applied to the modeling of conventional semiconducting alloys with small supercells that can be handled by traditional DFT systems [68]. This approach seeks to reduce the discrepancy between the correlation functions in a tiny supercell and those in an alloy with really random structure. Recently, the SQS approach has been widely employed to simulate the structures of metallic HEAs with a solid solution phase [69]. Here we give attention on SiGeSn HEA with the highest possible Sn content, which is 33% of the whole alloy composition. We create a SQS structure for the 216-atom SiGeSn HEA based on an MC process using the mcsqs module [70] implemented in the Alloy Theoretical Automated Toolkit (ATAT) package [71] (equivalent to a 3 3 3 supercell of the 8-atom unit cell of Si, Ge, or α-Sn). Figure 5 shows a zoomed-in view of the optimized SQS structure. As clearly shown. These results represent the SiGeSn HEA with a random solid solution phase. A 3 × 3 × 3 supercell of the SiGeSn alloy structure (5832 atoms) was used in the MD simulations, with the periodic boundary conditions applied in x, y, and z directions. The integration algorithm selected was the Velocity-Verlet algorithm with an integration

time-step of 1 fs. The initial temperatures for each volume covered the range from 3000 K to 6000 K with a step of 500 K. To vary the pressure, several densities, from 4.51 to 5.15 g/cm^3 were used. A simulation time of 1 ns (1×10^6 steps) was chosen for all SiGeSn HEA simulations.

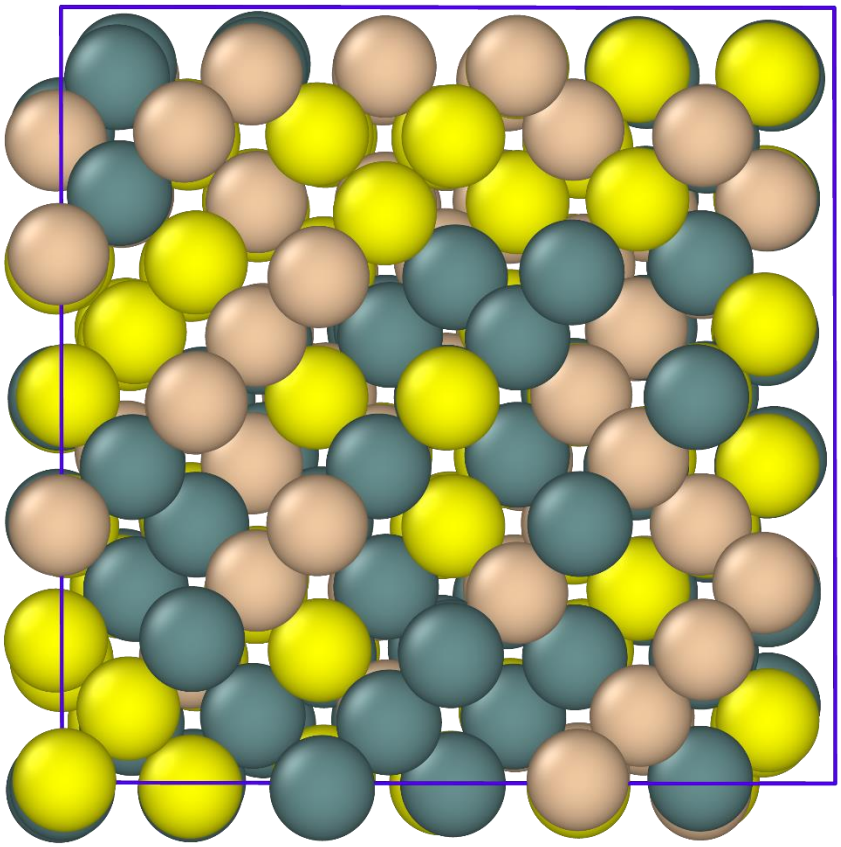

Figure 5. SiGeSn high entropy alloy structure.

Table 1. Stillinger-Weber (SW) potential Parameters for SiGeSn alloy (Tomita et al., 2018).

i	j	k	ε	σ	a	λ	γ	$\cos\theta$	A	B	P	q	tol
Unary parameters													
Si	Si	Si	1	2.095	1.8412	27.942	1.1495	-0.3333333	11.427	0.6729	4.4751	0.7277	0
Ge	Ge	Ge	1	2.181	1.811	32.101	1.1718	-0.3333333	10.093	0.6862	4.6973	0.6588	0
Sn	Sn	Sn	1	2.503	1.7825	28.747	1.161	-0.3333333	9.4315	0.7012	4.9827	0.6252	0
Binary parameters													
Si	Si	Ge	1	2.138	1.8568	10.057	0.9755	-0.3333333	0	0	0	0	0
Si	Ge	Si	1	2.138	1.8568	10.057	0.8574	-0.3333333	0	0	0	0	0
Si	Ge	Ge	1	2.138	1.8568	25.372	1.1877	-0.3333333	11.902	0.7189	4.4283	1.1451	0
Ge	Si	Si	1	2.138	1.8568	25.372	1.1877	-0.3333333	11.902	0.7189	4.4283	1.1451	0
Ge	Si	Ge	1	2.138	1.8568	24.845	1.3061	-0.3333333	0	0	0	0	0
Ge	Ge	Si	1	2.138	1.8568	24.845	1.0702	-0.3333333	0	0	0	0	0
Ge	Ge	Sn	1	2.337	1.7988	29.858	1.8136	-0.3333333	0	0	0	0	0
Ge	Sn	Ge	1	2.337	1.7988	29.858	0.7232	-0.3333333	0	0	0	0	0
Ge	Sn	Sn	1	2.337	1.7988	24.46	1.1484	-0.3333333	9.8864	0.7021	4.8537	0.6482	0
Sn	Ge	Ge	1	2.337	1.7988	24.46	1.1484	-0.3333333	9.8864	0.7021	4.8537	0.6482	0
Sn	Ge	Sn	1	2.337	1.7988	26.074	1.3564	-0.3333333	0	0	0	0	0
Sn	Sn	Ge	1	2.337	1.7988	26.074	1.0924	-0.3333333	0	0	0	0	0
Si	Si	Sn	1	2.337	1.7458	34.032	1.9639	-0.3333333	0	0	0	0	0
Si	Sn	Si	1	2.337	1.7458	34.032	0.695	-0.3333333	0	0	0	0	0
Si	Sn	Sn	1	2.337	1.7458	16.077	0.9447	-0.3333333	9.9807	0.6145	4.6433	0.2754	0
Sn	Si	Si	1	2.337	1.7458	16.077	0.9447	-0.3333333	9.9807	0.6145	4.6433	0.2754	0
Sn	Si	Sn	1	2.337	1.7458	28.575	1.3047	-0.3333333	0	0	0	0	0
Sn	Sn	Si	1	2.337	1.7458	28.575	1.12	-0.3333333	0	0	0	0	0
Ternary parameters													
Ge	Si	Sn	1	2.337	1.7988	16.193	0.7844	-0.3333333	0	0	0	0	0
Ge	Sn	Si	1	2.337	1.7988	16.193	1.3564	-0.3333333	0	0	0	0	0
Si	Ge	Sn	1	2.337	1.7458	26.645	1.1949	-0.3333333	0	0	0	0	0
Si	Sn	Ge	1	2.337	1.7458	26.645	1.3047	-0.3333333	0	0	0	0	0
Sn	Si	Ge	1	2.337	1.7458	31.877	0.695	-0.3333333	0	0	0	0	0
Sn	Ge	Si	1	2.337	1.7458	31.877	0.7232	-0.3333333	0	0	0	0	0

3.2 Small-cell coexistence method

In the traditional coexistence method, a large cell that contains half solid, half liquid and an interface between them is simulated to infer the melting temperature of the simulated structure based on the stability of these coexisting phases. This setup usually requires a large enough simulation cell to maintain the stability of the coexisting phases, otherwise the system will end up in one of two states eventually because of interface thermal fluctuations. Applying this setup in density functional theory (DFT) framework is extremely time consuming and expensive; due to the large cell requirement.

The small-cell coexistence method is a theoretical farmwork that solves the original method's issue and provides a more efficient and faster alternative [72]. The method's precise details and derivations can be found in a prior work, which we briefly outline below [72]. In small systems, the coexistence simulation evolves to one single state eventually, a liquid state or a solid state, due to the fluctuation of the system. In this method, the melting points are rigorously inferred based on statistical analysis of the fluctuations in the system. The general procedure is summarized in figure 6. To prepare a variety of distinct configurations (snapshots) of half-half solid-liquid coexistence, the super cell's other half is heated and melted first. The NPT MD is launched from these snapshots. For small system sizes, the two-phase coexistence quickly changes to a single-phase equilibrium, either completely solid or completely liquid, with a probability

defined by the system's temperature in relation to its melting point. The solid–liquid probability distributions P_{solid} and P_{liquid} follow the relations

$$\frac{P_{liquid}}{P_{solid}} = \exp(-G^{l-s}(T) l_x / (2k_B T)) \tag{1.43}$$

$$H^{s/l}(T) = H^{s/l}(T_m) + C_p^{s/l}(T - T_m) \tag{1.44}$$

$$S^{s/l}(T) = S^{s/l}(T_m) + C_p^{s/l} \ln \frac{T}{T_m} \tag{1.45}$$

$$G^{l-s}(T) = G^{l}(T) - G^{s}(T) = \frac{(T_m - T)}{T_m} H^{l-s}(T) - C_p^{l-s}(T) \frac{(T - T_m)^2}{T_m} \tag{1.46}$$

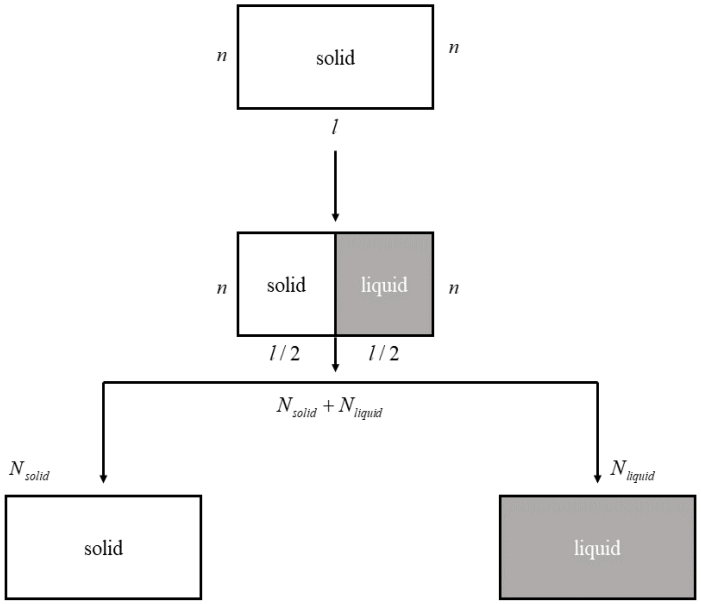

Figure 6. Schematic representation of the small-cell coexistence approach in action.

Detailed derivation of Eq. 1.43 and its validation can be found in Ref. [72] and are omitted here. Through fitting, we obtain melting properties, e.g., melting point T_m, solid

and liquid enthalpies $H^{s/l}(T_m)$ at T_m and heat capacities $C_p^{l-s}(T)$. Here G is Gibbs free energy, S is entropy and l_x is a finite-size parameter

3.2.1 DFT Calculations in the SLUSCHI code

A free automated computer code called SLUSCHI has been developed for the small-cell coexistence method used in direct DFT melting point calculations [73]. With an interface to the first-principles code VASP, SLUSCHI is a completely automated code that determines melting points using first-principles molecular dynamics simulations. SLUSCHI will automatically create a supercell of the right size, prepare solid-liquid coexistence, and then apply the small-cell coexistence method to determine the melting temperature starting from the crystal structure of a solid (which the user inputs). Because DFT calculations are highly generalizable, SLUSCHI code can be used to almost any kind of materials. Projector-augmented-wave (PAW) implementation and the generalized gradient approximation (GGA) for exchange-correlation energy in the Perdew, Burke, and Ernzerhof form were utilized for the DFT calculations in the Vienna Ab initio Simulation Package (VASP). Because the simulations were run at high temperatures, we used proper pseudo-potentials and considered the semicore s and p states as valence states. We apply the code to study these melting points of SiGe and SiGeSn alloys and compare the results with the empirical interatomic potential calculations from classical molecular dynamics. Similar to the classical MD simulations, we start this calculation by generating a SQS structure that represents the random HEA alloy. We generate a SQS structure of SiGeSn HEA with 54 atoms (18 atoms of each element) and also for

accuracy, we generate a SQS for binary SiGe alloy with 64 atoms (32 atoms of each element).

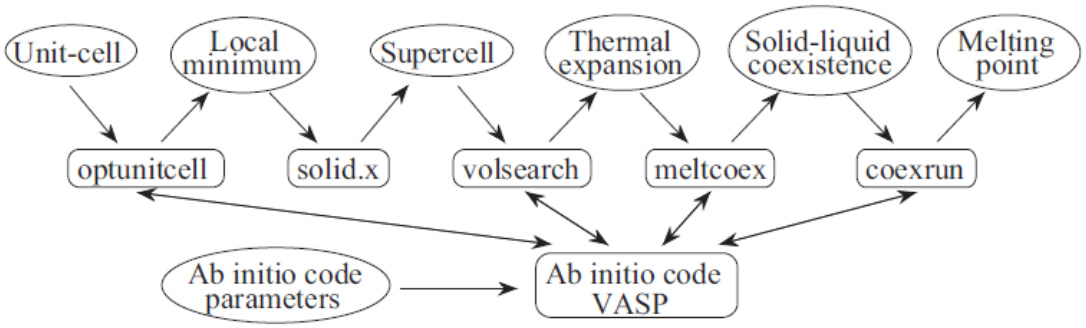

Figure 7. A diagram of SLUSCHI. Individual steps are carried out in sequence to approach the melting point. Interaction with VASP is heavily employed.

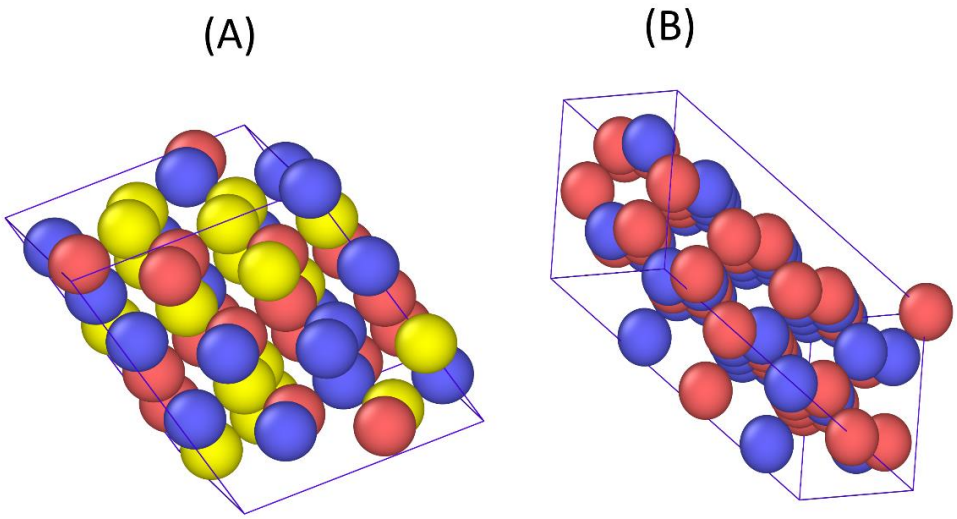

Figure 8. SQS Alloy Structures used DFT simulations. (A) SiGeSn HEA and (B) SiGe binary alloy.

4 RESULTS AND DISCUSSION

4.1 Z-Method Calculations

The Z-method method is a computational single-phase method for melting curve prediction of materials. The method has been extensively applied in many melting using classical [74-81] or Ab initio molecular dynamics [65, 82-93] . Although this method has proven to be a good alternative to other more complex procedures like the coexistence method, because of its simple simulation protocol and the ability to apply it on small systems, it has many documented drawbacks that affect its reliability and accuracy. Melting in nature is usually initiated at surfaces and crystal defects (heterogenous melting). In comparison, homogenous melting is a rare-event process, and it's by no means the same. The issues can be summarized in two points: (1) superheating (hysteresis) effect and (2) waiting times. In the Z-method, the ideal crystal structure remains in a metastable solid state even after passing its melting point and then it reaches its limit of superheating, after that, any increase in the temperature will cause the structure to melt and naturally decrease its temperature to the melting temperature. However, the amount of extra energy given to the system determines the extent of superheating, and hence the calculation error. This is the so-called hysteresis phenomenon, and it results in a significant overestimation of the melting point, even for simple monatomic molecules. Another prominent issue is the melting waiting time. Since The chance to form a nucleation center depends not only on the activation energy, but also the amount of time elapsed. In this framework, how long is the waiting time until the melting occurs? Studies by Alfe et al. [94], Davis et al. [95] and Lee et al. [96] showed

the heavy dependance of the melting waiting time in the Z method on the system size (number of atoms) and temperature, and that it can be subject to large errors if it is applied to small systems over short times. In the literature, studies that apply the Z-method in the Ab initio framework tend to have more successful and realistic melting curves compared with studies that use classical interatomic potentials. This is expected due to the empirical nature of the interatomic potentials. However, applying a full a series of DFT calculations in a procedure like the Z-method can be a quite expensive and time-consuming procedure for a large system such as SiGeSn HEA. With that in mind, we choose to apply the Z-method in classical MD framework using the available empirical potentials, and see the result before transitioning to full ab initio model.

4.1.1 Method and Interatomic Potential Validation

To our knowledge, there are two currently available classical interatomic potentials developed for SiGeSn alloys, one developed by Tomita et al. [67] and another developed by Lee et al. [97]. First, we test the Z-method using the same classical MD simulations setup for both of the potentials to see their success. The model developed by Lee et al. failed to produce any Z-method isochores using the standard Z-method protocol and it just gives a T-P plot that is monotonically increasing. This excludes this potential from usage in this study. The other potential developed by Tomita et al., successfully produces Z-method isochores and its results are shown in the next section 4.1.2 of this thesis. To test the reliability of the Z-method for SiGeSn alloy and its sub-systems, and the interatomic potential used in this study, we apply the Z-method melting curve calculation on the pure and binary SiGeSn systems using the same potential and other

available test potentials for each case. The pure element structures were created using the *lattice* command as a diamond lattice in the LAMMPS code. Si, Ge and Sn used lattice parameters were 5.43 Å, 5.66 Å and 6.489 Å. The binary alloys starting structures were created in LAMMPS as an ordered diamond lattice with eight basis, filling half of the basis with each element type. After that, the systems were replicated using the *region* and *replicate* commands to create a 2744 atom structures for all pure elements and binary alloy simulations. Several initial volumes that correspond to different system densities were chosen, and an initial temperature range of 3000 K to 6000 K, with a step of 500 K. The integration time-step was 1 fs with a simulation time of 250 ps. The results of these calculations are summarized in Table 2 and Figure 10 and 11. We find that using the Stillinger-Webber potential developed by Tomita et al. [67], the Z-method fails to produce any isochore plots for the Si, Ge, and Sn pure element systems. For the binary systems, the used potential can produce Z-method isochores for SiGe and GeSn only, and it can't produce any isochores for the SiSn system. For the SiGe system, which has a known experimental melting point of 1473 K at ambient pressure, we get a melting point of 1486 K at 0.37 GPa, which is just slightly higher than the experimental value of 1473 at 0 GPa [27, 98]. We also test all other available potential forms available for Ge and Sn, like Tersoff potential for Ge [99], and MEAM potential for Ge [100] and Sn [101] and they all fail to produce any melting isochores using the Z-method. In a previous study, Silicon melting curve has been investigated using the Z-method with multiple interatomic potentials [74]. Although the interatomic potentials successfully produced Z-method

isochores, none of the tested potentials is able to reproduce the experimental melting curve of silicon by means of the Z-method as reported by the study.

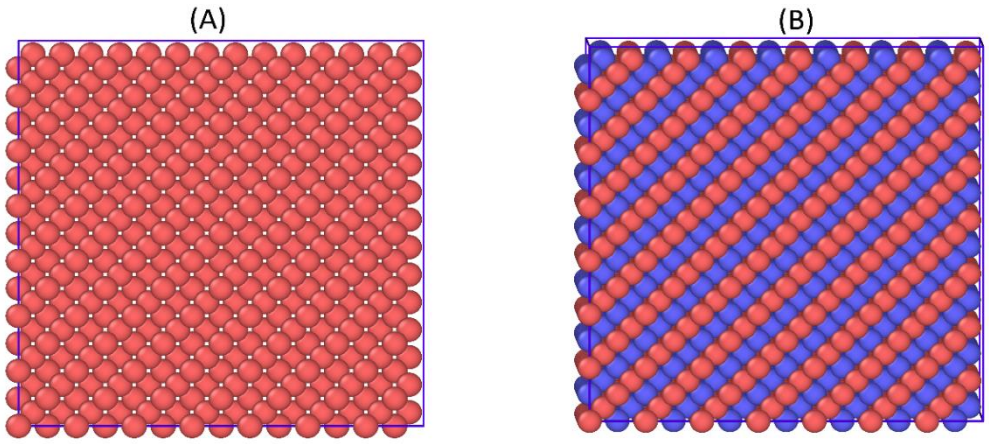

Figure 9. Examples of the created structures in LAMMPS for the testing of the Z-method. (A) Si structure and (B) SiGe binary alloy structure. Other pure elements and binary alloys have the same kind of structures appearing in this figure but with different lattice constants.

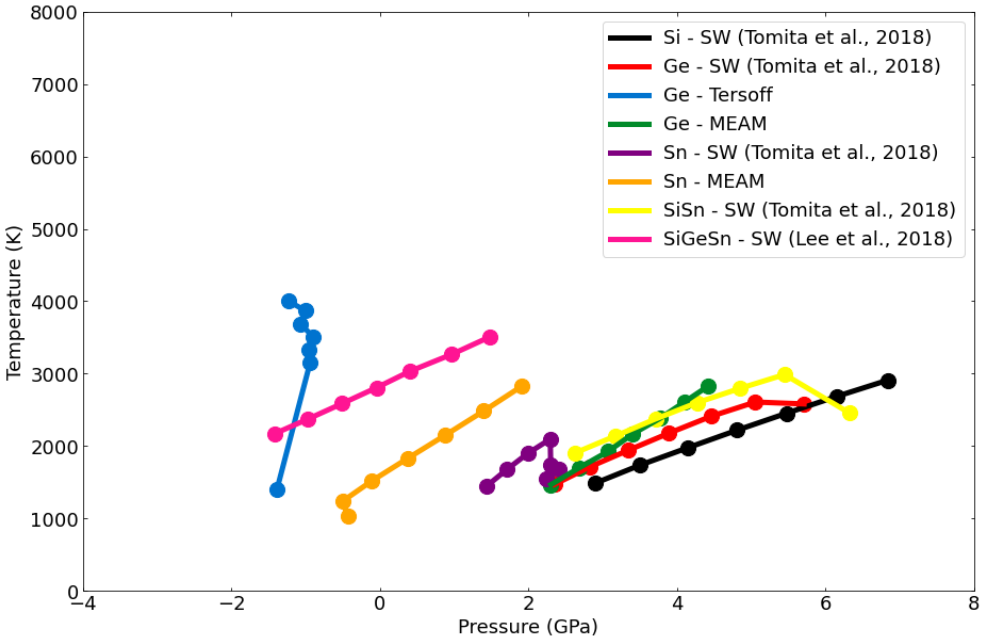

Figure 10. T vs P plot for all failed Z-method attempts on the SiGeSn systems using different interatomic potentials. The standard Z-method isochore should have a shape like the letter “Z” to obtain a melting point which is not the case in all of these curves.

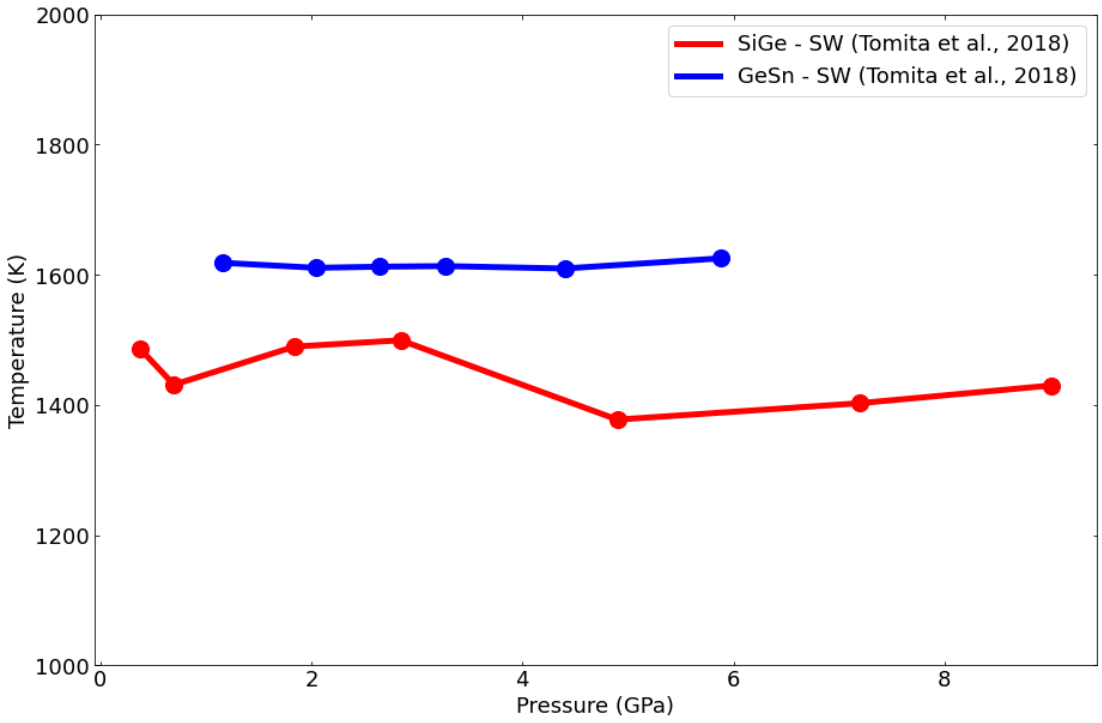

Figure 11. Melting Curves of the successful Z-method calculations for SiGe and GeSn binary alloy systems. Unlike failed attempts where there is only one T vs P plot to prove failure (not showing Z curve), each point on this plot was taken from a complete isochore that has a "Z" shape and an estimate of the melting point at a certain pressure. The collection of these melting points for each alloy is what is shown in this figure.

Table 2. Summary of the Z-method results for SiGeSn systems

Structure	Interatomic potential used	Z-Method status
Si	SW (Tomita et al., 2018) – This work	Failed
Si	SW – (Felipe González-Cataldo et al., 2018) work	Succeeded
Si	EDIP – (Felipe González-Cataldo et al., 2018) work	Succeeded
Si	Tersoff MOD – (Felipe González-Cataldo et al., 2018) work	Succeeded
Si	Tersoff T3 – (Felipe González-Cataldo et al., 2018) work	Succeeded

Ge	SW (Tomita et al., 2018) – This work	Failed
Ge	Tersoff – This work	Failed
Ge	MEAM – This work	Failed
Sn	SW (Tomita et al., 2018) – This work	Failed
Sn	MEAM – This work	Failed
SiGe	SW (Tomita et al., 2018) – This work	Succeeded
SiSn	SW (Tomita et al., 2018) – This work	Failed
GeSn	SW (Tomita et al., 2018) – This work	Succeeded
SiGeSn	SW (Tomita et al., 2018) – This work	Succeeded
SiGeSn	SW (Lee et al., 2018) – This work	Failed

4.1.2 Z-method isochores for SiGeSn alloy

Using the Stillinger-Weber potential developed by Tomita et al. for the SiGeSn alloy, the Z-method successfully produces isochores plots. The isochore plots obtained from the Z-method simulations of SiGeSn alloy are shown in figure. Each point on the plot represents a separate simulation of SiGeSn alloy, at a certain density but with different starting kinetic energy (different initial temperature given to the overall crystal structure at the start of the simulation). Each temperature and pressure point of this plot represents an average of the last 50 time-steps of that simulation, taken from the LAMMPS log file, ensuring the data taken are data points after reaching full equilibrium. The lowest point on the *liquid branch* (which is drawn as a diamond shape in the plots) can be taken as a good estimate for the melting temperature.

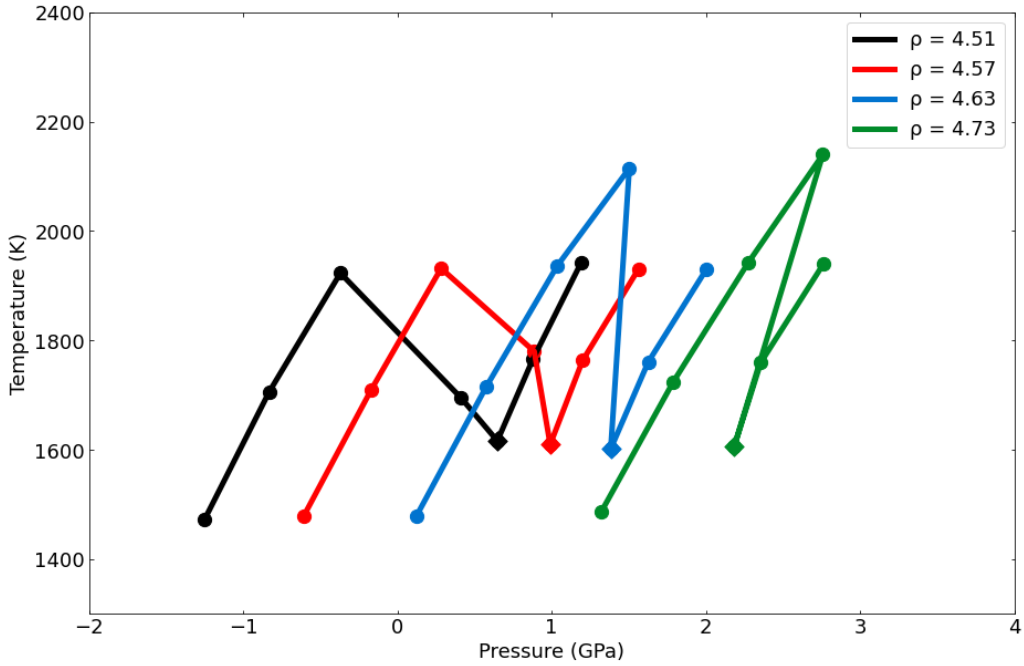

Figure 12. First group of the Z method isochores for the SiGeSn HEA. The diamond shaped point is the point representing the estimate for the melting point from each isochore.

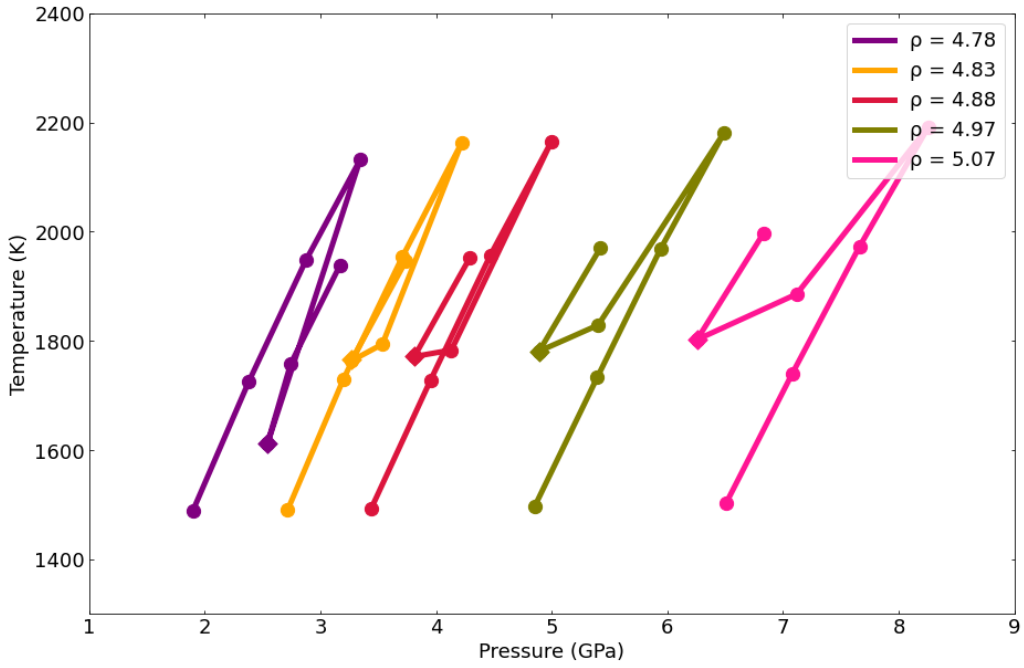

Figure 13. Second group of the Z method isochores for the SiGeSn HEA. The diamond shaped point is the point representing the estimate for the melting point from each isochore.

4.1.3 Size and simulation time effects

To verify that we reached the thermodynamic equilibrium at the critical superheating and the melting temperature, we check the effects of the structure size and the simulation time on the final result of the isochore. We take the structure with a density of 4.51 g/cm^3 as an example and use it to check the effect of simulation size and time. We check the simulation size effect by doing one simulation with a size of 13824 atoms and the simulation time effect by increasing the time to 1250 ps and see the results for isochore points around the melting point. We can see clearly from Figure 14 that any simulation size or time that are bigger than 5832 atoms and 1000 ps will result to almost

the same melting point value. This means that our used simulation size of 5832 atoms and time of 1000 ps are sufficient to calculate the melting isochores.

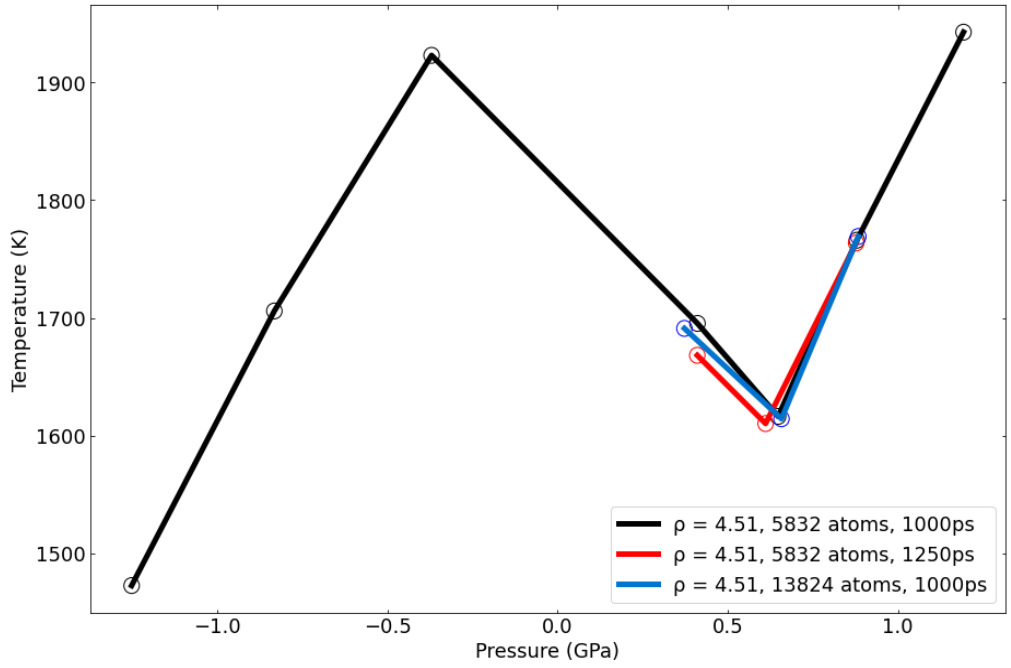

Figure 14. Simulation size and time effects for SiGeSn HEA Z-method simulations using the isochore at density 4.51 g.cm^3. No differences are appreciated in the prediction of the melting point.

4.1.4 Analysis of Z-method isochores

To verify that we indeed have a solid behavior at T_{LS} and a liquid behavior at T_m, we compare the mean squared displacement (MSD) as a function of time for the atoms. For instance, for the density 4.51 g/cm^3 (Figure 15), the behavior of the mean squared displacement as a function of time for four different temperatures (which are labeled on Figure 15) two from the solid branch, which are $T = 1705K$ and $T = 1922K$ which corresponds to the critical superheating temperature T_{LS} (where solid like diffusion is

expected) and two from the liquid branch $T = 1616K$ which corresponds to the melting temperature T_m (where liquid like diffusion is expected) and $T = 1765K$ is shown in Figure 16. The difference in the diffusion behavior (which is related to the slope of MSD vs. t graph) is clear. At T_m, the MSD is linearly increasing with time, as predicted for liquids, while at T_{LS}, the MSD reaches a constant value as the atoms in the solid cannot diffuse away from their equilibrium positions in the crystal.

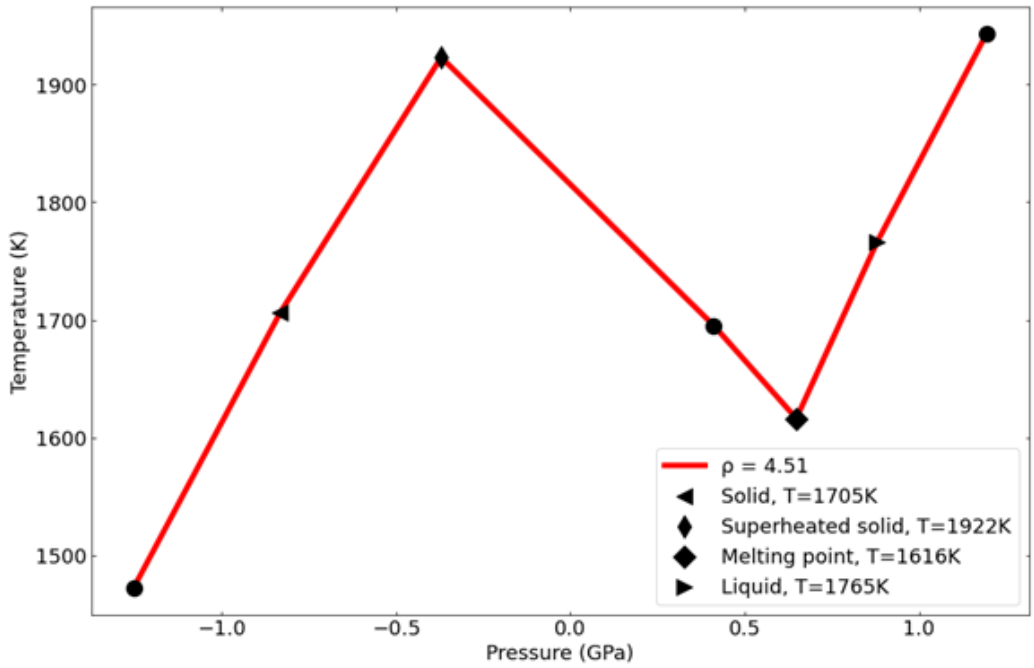

Figure 15. Detailed analysis of the isochore at density 4.51 g/cm^3.

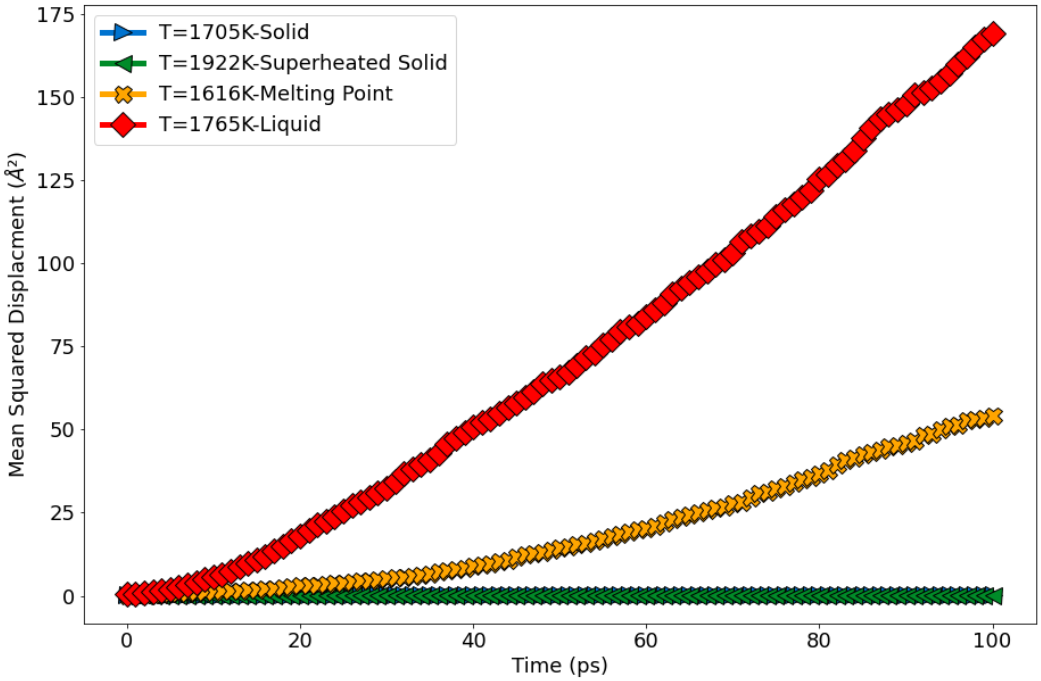

Figure 16. Mean square displacement (MSD) of SiGeSn atoms as a function of time from different simulations at different points from the 4.51 g/cm^3 density isochore. We can see a distinct behavior between MSD of simulation at melting point and liquid branch compared to the critical superheating point and the solid branch.

To further characterize the solid and liquid states obtained, the radial distribution function (RDF) for the final structure of each simulation was calculated.

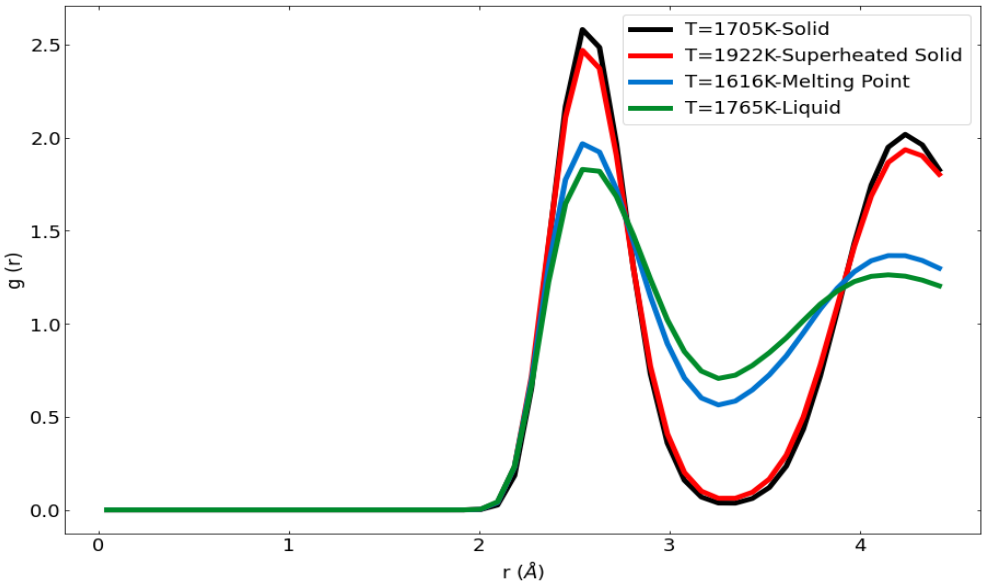

Figure 17. Radial distribution function of SiGeSn atoms from different simulations at different points from the 4.51 g/cm^3 density isochore. We can see a distinct behavior between RDF of simulation at melting point and liquid branch compared to the critical superheating point and the solid branch.

Figure 18 shows the alloy structure in four different points: (A) final structure of the simulation at $T = 1705K$, (B) final structure of T_{LS} simulation (C) final structure of T_m simulation and (D) final structure of the simulation at $T = 1765K$. We can see that in the T_{LS} simulation, the final structure still has its crystalline nature with a little bit of distortion, while in T_m, the structure lost any form of crystallinity in it, which is consistent with the MSD and RDF plots.

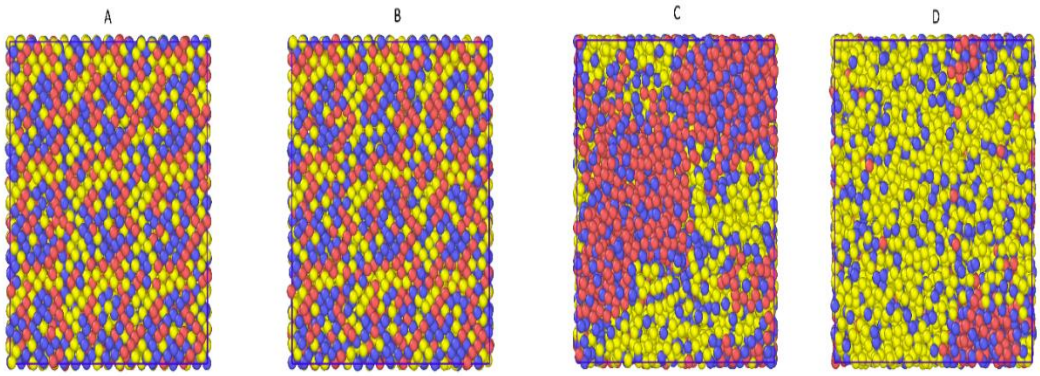

Figure 18. SiGeSn HEA alloy structure in four different points: (A) final structure of the simulation at $T = 1705K$, (B) final structure of T_{LS} simulation (C) final structure of T_m simulation and (D) final structure of the simulation at $T = 1765K$.

4.1.5 Melting curve from molecular dynamics simulations

The melting points obtained from each isochore and their corresponding pressure are shown in Table 3. The obtained melting curve is shown in figure.

Table 3. Melting curve data of SiGeSn HEA up to 6 GPa from the Z-method simulations

T_m (K)	P_m (GPa)
1616	0.65
1609	1
1601	1.38
1605	2.18
1611	2.54
1763	3.27
1771	3.81
1781	4.89
1802	6.26

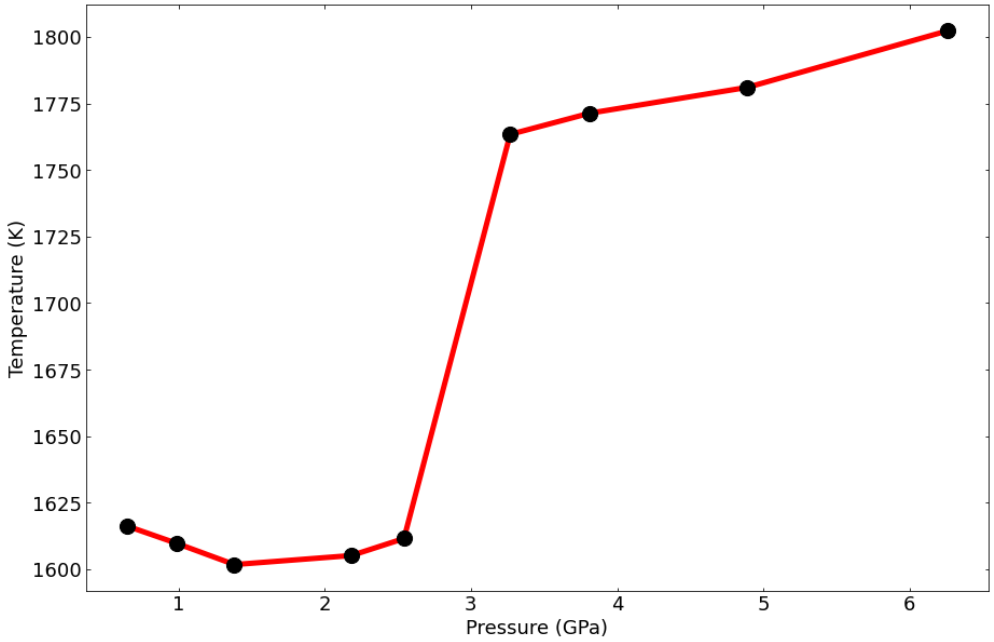

Figure 19. Melting curve of SiGeSn HEA up to 6 GPa from the Z-method simulations

This melting curve has a sharp increase, which is something common in the Z-method melting curves. Since this ternary structure hasn't been synthesized or studied experimentally in its HEA form, we have no experimental data to compare with. However, considering that the melting points of Si, Ge and Sn in K are 1,683, 1,211 and 505.1, respectively, and each of these elements make 33% of the alloy composition, it's highly unlikely that this melting curve result from the Z-method classical MD represents accurate melting curve data. One observation from this data is that any binary or ternary interatomic potential that included the element Sn in it had a tendency to fail or predict completely inaccurate melting points.

4.1.6 Conclusions from molecular dynamics simulations

From the results of this study, we conclude that none of the available classical interatomic potentials for SiGeSn is valid to use in melting studies using the Z-method. The quality of empirical potentials for Group IV elements should be revised and further studied in order to develop models that are accurate enough to use for melting studies in classical molecular dynamics, especially with models that contain high Sn content where not much work have been done to model their behavior.

4.2 DFT Calculations using the SLUSCHI code

The small-cell coexistence method was developed based on the need for efficient and reliable DFT melting point calculation method. The accuracy (typically with an error smaller than 100 K), robustness and efficiency of the method have been demonstrated in a range of materials [72, 73, 102-105], including a multi-principal component Mo–Ru–Ta–W HCP alloy [104]. In particular, the small-cell coexistence method and the SLUSCHI code was employed to computationally predict the material with the highest melting point, which was subsequently confirmed by independent experiments [106-108]. We Note that in this work, we used the conventional PBE exchange correlation functionals, which usually underestimates the melting point, due to its underbinding nature. So, each melting temperature we calculate here would be underestimated by about at least 200K-350K, as we will see in the next sections. To get an accurate melting point for SiGeSn systems, the use hybrid functionals such as HSE is required

4.2.1 SiGeSn HEA alloy

We study the melting point of SiGeSn HEA using DFT small-cell coexistence method to obtain a more reliable result and to compare it with the results from the Z-method. We choose to calculate the melting point at the ambient pressure (1 bar). Starting from the generated SQS structure, that structure is fed into the SLUSCHI code. Duplicates of half solid- half-liquid coexistence simulations were carried out at various temperatures, and solid–liquid probability distribution was analyzed to rigorously infer the final melting temperature. The calculated meting point of SiGeSn is 754 ± 46 K.

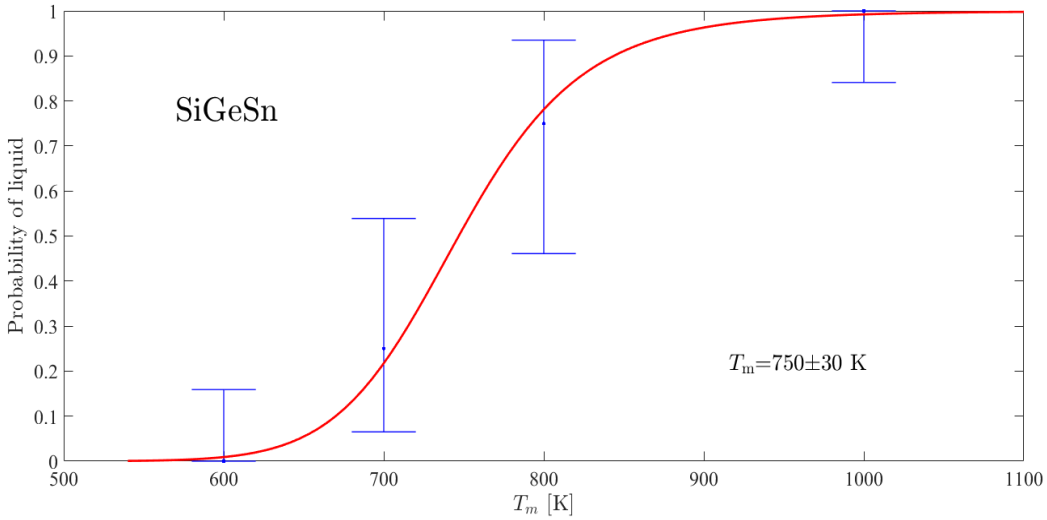

Figure 20. Melting temperature calculation for SiGeSn HEA. Error bars represent the standard error of binomial distribution.

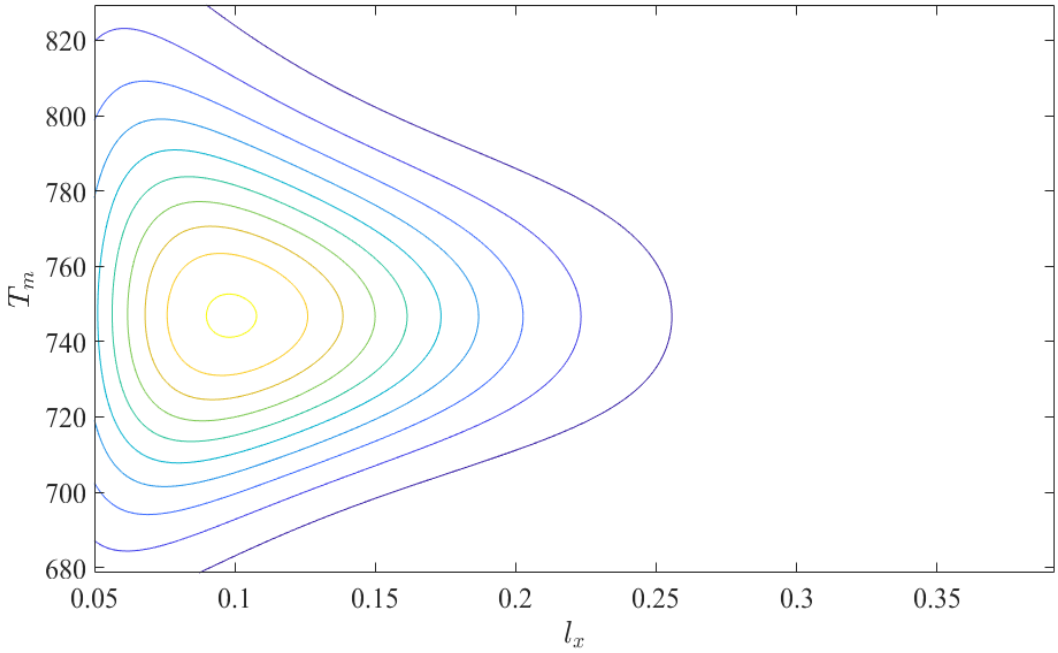

Figure 21. A 2-D contour of the likelihood function for SiGeSn melting point, which provides the mean and the standard deviation of the melting point.

4.2.2 SiGe binary alloy

The ambient pressure melting point of the binary SiGe alloy was calculated using the SLUSCHI code. Duplicates of half solid- half-liquid coexistence simulations were carried out at various temperatures, and solid–liquid probability distribution was analyzed to rigorously infer the final melting temperature. The calculated meting point of SiGe is 1174 ± 16 K. While this melting point is lower than the experimental melting point of 1487K, the HSE correction for this calculation is expected to raise this melting temperature by around 200-300K, which will make it around the correct melting temperature for this alloy.

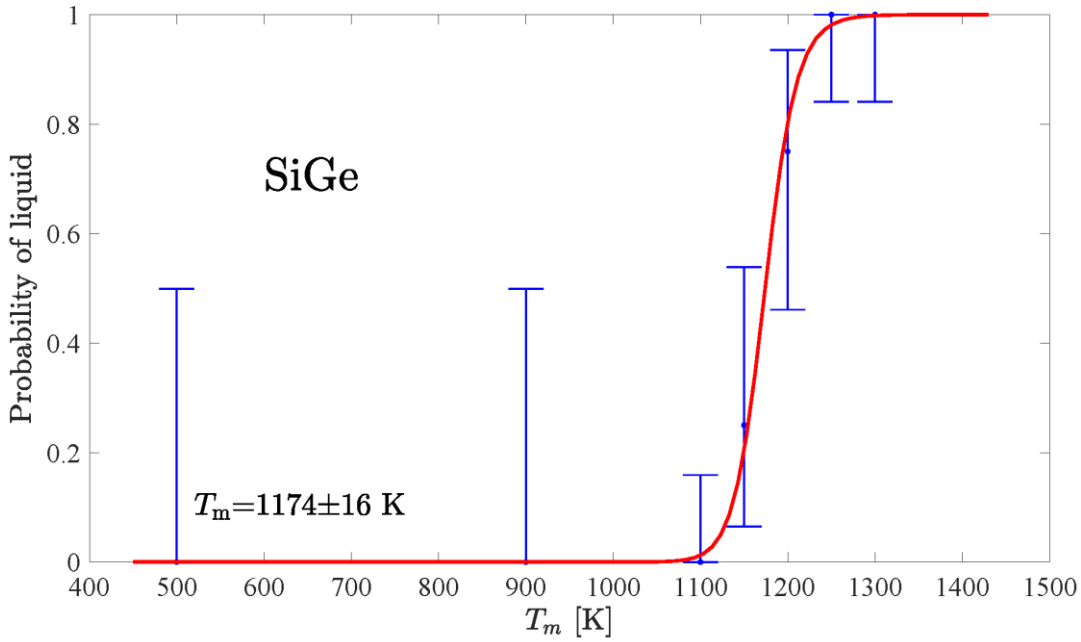

Figure 22. Melting temperature calculation for SiGe binary alloy.

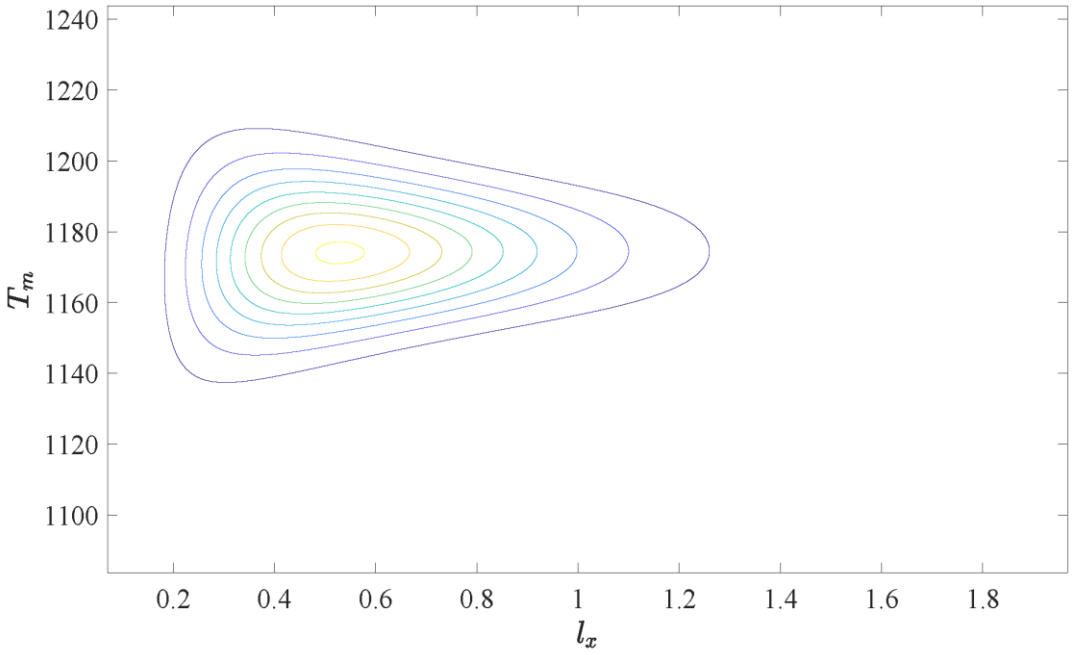

Figure 23. A 2-D contour of the likelihood function for SiGe melting point, which provides the mean and the standard deviation of the melting point.

4.2.3 Conclusions from DFT calculations

The used DFT model predicts overall more accurate melting temperatures. Since DFT calculations give a melting temperature way below 1600K for the SiGeSn HEA, we believe the actual melting temperature of SiGeSn is indeed below 1600K, and the empirical potential could be wrong. As mentioned before, Sn does not like mixing with Ge and Si. The binary Si, Ge and Sn phase diagrams demonstrates this fact. This explains why the ternary SiGeSn is so unstable. HSE correction for these DFT calculations is expected to raise the melting temperatures of SiGe and SiGeSn to around 1474K and 1050K, respectively.

5 CONCLUSIONS AND FUTURE WORK

In this work, the melting point of $Si_{0.5}Ge_{0.5}$ binary and $Si_{0.3}Ge_{0.3}Ge_{0.3}$ high entropy alloy was studied using the Z-method and small-cell coexistence method in the classical and ab-initio molecular dynamics farmwork. From classical molecular dynamics Z-method simulations, we concluded that none of the available empirical potentials is able to produce any reasonable melting point for the SiGeSn HEA or any of its subsystems. The accuracy and quality of Group IV empirical should be further tested and developed in order for these potentials to capture solid and liquid states correctly and predict accurate melting points. The DFT calculations gave more reasonable and accurate melting points for both the binary and ternary high entropy alloy, which were 1174 ± 16 and 754 ± 46 K, respectively. We note that these calculations were done using the PBE exchange-correlation functionals, which usually underestimates their melting points. Using hybrid energy functionals such as HSE would raise the melting temperatures for SiGe and SiGeSn HEA to around 1474K and 1050K, respectively. For the SiGe alloy, this is almost exactly the experimentally melting point. For the SiGeSn HEA, the melting point is very close to the expected mean melting point when these three elements combined in a single structure. While the SiGeSn HEA has shown some exceptional semiconducting and thermoelectric properties in previous computational studies, the melting point of this alloy doesn't show any unregular deviation from the expected melting point when these three elements are combined together. However, the melting point is still appropriate for the intended applications of this alloy in Optoelectronics. The promising properties of this alloy encourage future experimental synthesis and further

development of simulation models to obtain more accurate thermal transport properties for these HEAs.

BIBLIOGRAPHY

1. Yeh, J.W., et al., *High-Entropy Alloys – A New Era of Exploitation.* Materials Science Forum, 2007. **560**: p. 1-9.

2. Miracle, D.B., *High entropy alloys as a bold step forward in alloy development.* Nat Commun, 2019. **10**(1): p. 1805.

3. Ye, Y.F., et al., *High-entropy alloy: challenges and prospects.* Materials Today, 2016. **19**(6): p. 349-362.

4. Gorsse, S., J.-P. Couzinié, and D.B. Miracle, *From high-entropy alloys to complex concentrated alloys.* Comptes Rendus Physique, 2018. **19**(8): p. 721-736.

5. Yeh, J.-W., et al., *Nanostructured High-Entropy Alloys with Multiple Principal Elements: Novel Alloy Design Concepts and Outcomes.* Advanced Engineering Materials, 2004. **6**(5): p. 299-303.

6. Cantor, B., et al., *Microstructural development in equiatomic multicomponent alloys.* Materials Science and Engineering: A, 2004. **375-377**: p. 213-218.

7. Takeuchi, A. and A. Inoue, *Classification of Bulk Metallic Glasses by Atomic Size Difference, Heat of Mixing and Period of Constituent Elements and Its Application to Characterization of the Main Alloying Element.* MATERIALS TRANSACTIONS, 2005. **46**(12): p. 2817-2829.

8. Zhang, Y., et al., *Solid-Solution Phase Formation Rules for Multi-component Alloys.* Advanced Engineering Materials, 2008. **10**(6): p. 534-538.

9. Zhang, Y., et al., *Microstructures and properties of high-entropy alloys.* Progress in Materials Science, 2014. **61**: p. 1-93.

10. Guo, S., et al., *Effect of valence electron concentration on stability of fcc or bcc phase in high entropy alloys.* Journal of Applied Physics, 2011. **109**(10): p. 103505.

11. Yeh, J.W., *Recent progress in high-entropy alloys.* Annales de Chimie Science des Materiaux (Paris), 2006. **31**(6): p. 633-648.

12. Yeh, J.-W., *Physical Metallurgy of High-Entropy Alloys.* JOM, 2015. **67**(10): p. 2254-2261.

13. Tong, C.-J., et al., *Mechanical performance of the AlxCoCrCuFeNi high-entropy alloy system with multiprincipal elements.* Metallurgical and Materials Transactions A, 2005. **36**(5): p. 1263-1271.

14. Zhou, Y.J., et al., *Solid solution alloys of AlCoCrFeNiTix with excellent room-temperature mechanical properties.* Applied Physics Letters, 2007. **90**(18): p. 181904.

15. Chen, M.-R., et al., *Effect of vanadium addition on the microstructure, hardness, and wear resistance of Al0.5CoCrCuFeNi high-entropy alloy.* Metallurgical and Materials Transactions A, 2006. **37**(5): p. 1363-1369.

16. Hemphill, M.A., et al., *Fatigue behavior of Al0.5CoCrCuFeNi high entropy alloys.* Acta Materialia, 2012. **60**(16): p. 5723-5734.

17. Tang, Z., et al., *Fatigue behavior of a wrought Al0.5CoCrCuFeNi two-phase high-entropy alloy.* Acta Materialia, 2015. **99**: p. 247-258.

18. Yang, T., et al., *Precipitation behavior of AlxCoCrFeNi high entropy alloys under ion irradiation.* Scientific Reports, 2016. **6**(1): p. 32146.

19. Lu, C., et al., *Enhancing radiation tolerance by controlling defect mobility and migration pathways in multicomponent single-phase alloys.* Nature Communications, 2016. **7**(1): p. 13564.

20. Gao, M.C., et al., *High-entropy functional materials.* Journal of Materials Research, 2018. **33**(19): p. 3138-3155.

21. Wang, X.F., et al., *Novel microstructure and properties of multicomponent CoCrCuFeNiTix alloys.* Intermetallics, 2007. **15**(3): p. 357-362.

22. Koželj, P., et al., *Discovery of a Superconducting High-Entropy Alloy.* Physical Review Letters, 2014. **113**(10): p. 107001.

23. Hu, L., et al., *Entropy Engineering of SnTe: Multi-Principal-Element Alloying Leading to Ultralow Lattice Thermal Conductivity and State-of-the-Art Thermoelectric Performance.* Advanced Energy Materials, 2018. **8**(29): p. 1802116.

24. Zaima, S., et al., *Growth and applications of GeSn-related group-IV semiconductor materials.* Science and Technology of Advanced Materials, 2015. **16**(4): p. 043502.

25. Moontragoon, P., Z. Ikonić, and P. Harrison, *Band structure calculations of Si–Ge–Sn alloys: achieving direct band gap materials.* Semiconductor Science and Technology, 2007. **22**(7): p. 742-748.

26. Kouvetakis, J., J. Menendez, and A.V.G. Chizmeshya, *TIN-BASED GROUP IV SEMICONDUCTORS: New Platforms for Opto- and Microelectronics on Silicon.* Annual Review of Materials Research, 2006. **36**(1): p. 497-554.

27. Olesinski, R.W. and G.J. Abbaschian, *The Ge−Si (Germanium-Silicon) system.* Bulletin of Alloy Phase Diagrams, 1984. **5**(2): p. 180-183.

28. Colace, L. and G. Assanto, *Germanium on Silicon for Near-Infrared Light Sensing.* IEEE Photonics Journal, 2009. **1**(2): p. 69-79.

29. Olesinski, R.W. and G.J. Abbaschian, *The Si-Sn (Silicon-Tin) system.* Bulletin of Alloy Phase Diagrams, 1984. **5**(3): p. 273-276.

30. Olesinski, R.W. and G.J. Abbaschian, *The Ge−Sn (Germanium−Tin) system.* Bulletin of Alloy Phase Diagrams, 1984. **5**(3): p. 265-271.

31. Wirths, S., D. Buca, and S. Mantl, *Si–Ge–Sn alloys: From growth to applications.* Progress in Crystal Growth and Characterization of Materials, 2016. **62**(1): p. 1-39.

32. Oehme, M., et al., *Epitaxial growth of highly compressively strained GeSn alloys up to 12.5% Sn.* Journal of Crystal Growth, 2013. **384**: p. 71-76.

33. Xie, J., et al., *Synthesis, Stability Range, and Fundamental Properties of Si−Ge−Sn Semiconductors Grown Directly on Si(100) and Ge(100) Platforms.* Chemistry of Materials, 2010. **22**(12): p. 3779-3789.

34. Chang, G., S. Chang, and S.L. Chuang, *Strain-Balanced <formula formulatype="inline"><tex Notation="TeX">${\rm Ge}_{z}{\rm Sn}_{1-z}\hbox{--}{\rm Si}_{x}{\rm Ge}_{y}{\rm Sn}_{1-x-y}$</tex></formula> Multiple-Quantum-Well Lasers.* IEEE Journal of Quantum Electronics, 2010. **46**(12): p. 1813-1820.

35. Aella, P., et al., *Optical and structural properties of SixSnyGe1−x−y alloys.* Applied Physics Letters, 2004. **84**(6): p. 888-890.

36. Bauer, M., et al., *Synthesis of ternary SiGeSn semiconductors on Si(100) via SnxGe1−x buffer layers.* Applied Physics Letters, 2003. **83**(11): p. 2163-2165.

37. Sun, G., R.A. Soref, and H.H. Cheng, *Design of an electrically pumped SiGeSn/GeSn/SiGeSn double-heterostructure midinfrared laser.* Journal of Applied Physics, 2010. **108**(3): p. 033107.

38. Wang, D., et al., *Semiconducting SiGeSn high-entropy alloy: A density functional theory study.* Journal of Applied Physics, 2019. **126**(22): p. 225703.

39. Wang, D., et al., *Electrical and thermal transport properties of medium-entropy SiyGeySnx alloys.* Acta Materialia, 2020. **199**: p. 443-452.

40. Lennard-Jones, J.E. and A.F. Devonshire, *Critical and co-operative phenomena. III. A theory of melting and the structure of liquids.* Proceedings of the Royal Society of London. Series A. Mathematical and Physical Sciences, 1939. **169**(938): p. 317-338.

41. Jin, Z.H., et al., *Melting Mechanisms at the Limit of Superheating.* Physical Review Letters, 2001. **87**(5): p. 055703.

42. Luo, S.-N., A. Strachan, and D.C. Swift, *Nonequilibrium melting and crystallization of a model Lennard-Jones system.* The Journal of Chemical Physics, 2004. **120**(24): p. 11640-11649.

43. Luo, S.-N. and T.J. Ahrens, *Superheating systematics of crystalline solids.* Applied Physics Letters, 2003. **82**(12): p. 1836-1838.

44. Siwick, B.J., et al., *An Atomic-Level View of Melting Using Femtosecond Electron Diffraction.* Science, 2003. **302**(5649): p. 1382-1385.

45. Sokolowski-Tinten, K., et al., *Femtosecond X-ray measurement of coherent lattice vibrations near the Lindemann stability limit.* Nature, 2003. **422**(6929): p. 287-289.

46. Morris, J.R., et al., *Melting line of aluminum from simulations of coexisting phases.* Physical Review B, 1994. **49**(5): p. 3109-3115.

47. Belonoshko, A.B., R. Ahuja, and B. Johansson, *Quasi--Ab Initio Molecular Dynamic Study of Fe Melting.* Physical Review Letters, 2000. **84**(16): p. 3638-3641.

48. Morris, J.R. and X. Song, *The melting lines of model systems calculated from coexistence simulations.* The Journal of Chemical Physics, 2002. **116**(21): p. 9352-9358.

49. Watt, S.W., et al., *A molecular dynamics simulation of the melting points and glass transition temperatures of myo- and neo-inositol.* The Journal of Chemical Physics, 2004. **121**(19): p. 9565-9573.

50. Schwegler, E., et al., *Melting of ice under pressure.* Proceedings of the National Academy of Sciences, 2008. **105**(39): p. 14779-14783.

51. Yoo, S., S.S. Xantheas, and X.C. Zeng, *The melting temperature of bulk silicon from ab initio molecular dynamics simulations.* Chemical Physics Letters, 2009. **481**(1): p. 88-90.

52. Yoo, S., X.C. Zeng, and S.S. Xantheas, *On the phase diagram of water with density functional theory potentials: The melting temperature of ice Ih with the Perdew–Burke–Ernzerhof and Becke–Lee–Yang–Parr functionals.* The Journal of Chemical Physics, 2009. **130**(22): p. 221102.

53. Luo, S.-N., et al., *Maximum superheating and undercooling: Systematics, molecular dynamics simulations, and dynamic experiments.* Physical Review B, 2003. **68**(13): p. 134206.

54. Zheng, L., S.-N. Luo, and D.L. Thompson, *Molecular dynamics simulations of melting and the glass transition of nitromethane.* The Journal of Chemical Physics, 2006. **124**(15): p. 154504.

55. de Wijs, G.A., G. Kresse, and M.J. Gillan, *First-order phase transitions by first-principles free-energy calculations: The melting of Al.* Physical Review B, 1998. **57**(14): p. 8223-8234.

56. Alfè, D., G.D. Price, and M.J. Gillan, *Iron under Earth's core conditions: Liquid-state thermodynamics and high-pressure melting curve from ab initio calculations.* Physical Review B, 2002. **65**(16): p. 165118.

57. Sugino, O. and R. Car, *Ab Initio Molecular Dynamics Study of First-Order Phase Transitions: Melting of Silicon.* Physical Review Letters, 1995. **74**(10): p. 1823-1826.

58. Kofke, D.A. and P.T. Cummings, *Quantitative comparison and optimization of methods for evaluating the chemical potential by molecular simulation.* Molecular Physics, 1997. **92**(6): p. 973-996.

59. Lee, J.-G. *Computational Materials Science: An Introduction*. 2011.

60. LeSar, R., *Introduction to Computational Materials Science: Fundamentals to Applications*. 2013, Cambridge: Cambridge University Press.

61. Thompson, A.P., et al., *LAMMPS - a flexible simulation tool for particle-based materials modeling at the atomic, meso, and continuum scales.* Computer Physics Communications, 2022. **271**: p. 108171.

62. Kresse, G. and J. Furthmüller, *Efficiency of ab-initio total energy calculations for metals and semiconductors using a plane-wave basis set.* Computational Materials Science, 1996. **6**(1): p. 15-50.

63. Kresse, G. and J. Furthmüller, *Efficient iterative schemes for ab initio total-energy calculations using a plane-wave basis set.* Physical Review B, 1996. **54**(16): p. 11169-11186.

64. Belonoshko, A.B., et al., *Melting and critical superheating.* Physical Review B, 2006. **73**(1): p. 012201.

65. Belonoshko, A.B., et al., *Molybdenum at High Pressure and Temperature: Melting from Another Solid Phase.* Physical Review Letters, 2008. **100**(13): p. 135701.

66. Burakovsky, L., et al., *High-Pressure---High-Temperature Polymorphism in Ta: Resolving an Ongoing Experimental Controversy.* Physical Review Letters, 2010. **104**(25): p. 255702.

67. Tomita, M., et al., *Development of interatomic potential of Ge(1−x−y)SixSny ternary alloy semiconductors for classical lattice dynamics simulation.* Japanese Journal of Applied Physics, 2018. **57**(4S): p. 04FB04.

68. Zunger, A., et al., *Special quasirandom structures.* Physical Review Letters, 1990. **65**(3): p. 353-356.

69. Gao, M.C., *High-Entropy Alloys: Fundamentals and Applications.* High-Entropy Alloys, 2016.

70. van de Walle, A., et al., *Efficient stochastic generation of special quasirandom structures.* Calphad, 2013. **42**: p. 13-18.

71. van de Walle, A., *Multicomponent multisublattice alloys, nonconfigurational entropy and other additions to the Alloy Theoretic Automated Toolkit.* Calphad, 2009. **33**(2): p. 266-278.

72. Hong, Q.-J. and A.v.d. Walle, *Solid-liquid coexistence in small systems: A statistical method to calculate melting temperatures.* The Journal of Chemical Physics, 2013. **139**(9): p. 094114.

73. Hong, Q.-J. and A. van de Walle, *A user guide for SLUSCHI: Solid and Liquid in Ultra Small Coexistence with Hovering Interfaces*. Calphad, 2016. **52**: p. 88-97.

74. González-Cataldo, F., F. Corvacho, and G. Gutiérrez, *Melting curve of Si by means of the Z-method.* Journal of Physics: Conference Series, 2018. **1043**(1): p. 012038.

75. Davis, S., et al., *Molecular dynamics simulation of zirconia melting.* Open Physics, 2010. **8**(5): p. 789-797.

76. Fomin, Y.D., *Melting line and thermodynamic properties of a supeionic compound SrCl2 by molecular dynamics simulation.* Physics and Chemistry of Liquids, 2022. **60**(1): p. 59-67.

77. Finney, A.R. and P.M. Rodger, *Applying the Z method to estimate temperatures of melting in structure II clathrate hydrates.* Physical Chemistry Chemical Physics, 2011. **13**(44): p. 19979-19987.

78. Davis, S.M., et al., *High-pressure melting curve of hydrogen.* J Chem Phys, 2008. **129**(19): p. 194508.

79. Benazzouz, B.K., A. Zaoui, and A.B. Belonoshko, *Determination of the melting temperature of kaolinite by means of the Z-method.* American Mineralogist, 2013. **98**(10): p. 1881-1885.

80. Mausbach, P., R. Fingerhut, and J. Vrabec, *Structure and dynamics of the Lennard-Jones fcc-solid focusing on melting precursors.* The Journal of Chemical Physics, 2020. **153**(10): p. 104506.

81. Belonoshko, A.B., et al., *Melting of a polycrystalline material.* The European Physical Journal Special Topics, 2013. **216**(1): p. 199-204.

82. Belonoshko, A.B. and A. Rosengren, *High-pressure melting curve of platinum from ab initio Z method.* Physical Review B, 2012. **85**(17): p. 174104.

83. Li, D.F., et al., *Melting curve of lithium from quantum molecular-dynamics simulations.* Europhysics Letters, 2011. **95**(5): p. 56004.

84. Belonoshko, A.B., et al., *MgO phase diagram from first principles in a wide pressure-temperature range.* Physical Review B, 2010. **81**(5): p. 054110.

85. Fischer, R.A., et al., *Equations of state in the Fe-FeSi system at high pressures and temperatures.* Journal of Geophysical Research: Solid Earth, 2014. **119**(4): p. 2810-2827.

86. Burakovsky, L., N. Burakovsky, and D.L. Preston, *Ab initio melting curve of osmium.* Physical Review B, 2015. **92**(17): p. 174105.

87. Baty, S.R., L. Burakovsky, and D. Errandonea, *Ab Initio Phase Diagram of Copper.* Crystals, 2021. **11**(5): p. 537.

88. Baty, S.R., L. Burakovsky, and D. Errandonea, *Ab initio phase diagram of silver.* Journal of Physics: Condensed Matter, 2021. **33**(48): p. 485901.

89. González-Cataldo, F., S. Davis, and G. Gutiérrez, *Melting curve of SiO2 at multimegabar pressures: implications for gas giants and super-Earths.* Scientific Reports, 2016. **6**(1): p. 26537.

90. Nguyen-Cong, K., et al., *First principles molecular dynamics simulations of high-pressure melting of diamond.* AIP Conference Proceedings, 2020. **2272**(1): p. 070010.

91. Li, D., P. Zhang, and J. Yan, *Ab initio molecular dynamics study of high-pressure melting of beryllium oxide.* Scientific Reports, 2014. **4**(1): p. 4707.

92. Bouchet, J., et al., *Melting curve of aluminum up to 300 GPa obtained through ab initio molecular dynamics simulations.* Physical Review B, 2009. **80**(9): p. 094102.

93. Baty, S.R., et al., *Ab Initio Phase Diagram of Chromium to 2.5 TPa.* Applied Sciences, 2022. **12**(15): p. 7844.

94. Alfè, D., C. Cazorla, and M.J. Gillan, *The kinetics of homogeneous melting beyond the limit of superheating.* The Journal of Chemical Physics, 2011. **135**(2): p. 024102.

95. Davis, S., C. Loyola, and J. Peralta, *Bayesian statistical modeling of microcanonical melting times at the superheated regime.* Physica A: Statistical Mechanics and its Applications, 2019. **515**: p. 546-557.

96. Lee, J.H., C. Kim, and M.E. Colvin, *Molecular Dynamics Studies of the Melting Kinetics of Superheated Crystals.* The Journal of Physical Chemistry C, 2022. **126**(8): p. 4199-4208.

97. Lee, Y. and G.S. Hwang, *Molecular dynamics investigation of the thermal conductivity of ternary silicon–germanium–tin alloys.* Journal of Physics D: Applied Physics, 2017. **50**(49): p. 494001.

98. Thompson, M.O., et al., *Rapid solidification studies of a model alloy system.* Applied Physics Letters, 1986. **49**(10): p. 558-560.

99. Mahdizadeh, S.J. and G. Akhlamadi, *Optimized Tersoff empirical potential for germanene.* Journal of Molecular Graphics and Modelling, 2017. **72**: p. 1-5.

100. Kim, E.H., Y.-H. Shin, and B.-J. Lee, *A modified embedded-atom method interatomic potential for Germanium.* Calphad, 2008. **32**(1): p. 34-42.

101. Ko, W.-S., et al., *Atomistic Simulations of Pure Tin Based on a New Modified Embedded-Atom Method Interatomic Potential.* Metals, 2018. **8**(11): p. 900.

102. Hong, Q.-J., et al., *Combined computational and experimental investigation of high temperature thermodynamics and structure of cubic ZrO2 and HfO2.* Scientific Reports, 2018. **8**(1): p. 14962.

103. Hong, Q.-J. and A. van de Walle, *Prediction of the material with highest known melting point from ab initio molecular dynamics calculations.* Physical Review B, 2015. **92**(2): p. 020104.

104. Miljacic, L., et al., *Equation of state of solid, liquid and gaseous tantalum from first principles.* Calphad, 2015. **51**: p. 133-143.

105. Hong, Q.-J., et al., *Theoretical prediction of high melting temperature for a Mo–Ru–Ta–W HCP multiprincipal element alloy.* npj Computational Materials, 2021. **7**(1): p. 1.

106. Cedillos-Barraza, O., et al., *Investigating the highest melting temperature materials: A laser melting study of the TaC-HfC system.* Scientific Reports, 2016. **6**(1): p. 37962.

107. Buinevich, V.S., et al., *Fabrication of ultra-high-temperature nonstoichiometric hafnium carbonitride via combustion synthesis and spark plasma sintering.* Ceramics International, 2020. **46**(10, Part B): p. 16068-16073.

108. Ushakov, S.V. and A. Navrotsky, *Carbides and Nitrides of Zirconium and Hafnium.* 2019. **12**(17).